The deep Arctic Ocean and Fram Strait in CMIP6 models

Céline Heuzé,[a] Hannah Zanowski,[b] Salar Karam,[a] and Morven Muilwijk[c]

[a] *Department of Earth Sciences, University of Gothenburg, Gothenburg, Sweden*

[b] *Department of Atmospheric and Oceanic Sciences, University of Wisconsin-Madison, Madison, US*

[c] *Norwegian Polar Institute, Tromsø, Norway*

The deep Arctic Ocean and Fram Strait in CMIP6 models

Céline Heuzé,[a] Hannah Zanowski,[b] Salar Karam,[a] and Morven Muilwijk[c]

[a] *Department of Earth Sciences, University of Gothenburg, Gothenburg, Sweden*

[b] *Department of Atmospheric and Oceanic Sciences, University of Wisconsin-Madison, Madison, US*

[c] *Norwegian Polar Institute, Tromsø, Norway*

Corresponding author: Céline Heuzé, celine.heuze@gu.se

ABSTRACT: Arctic sea ice loss has become a symbol of ongoing climate change, yet climate models still struggle to reproduce it accurately, let alone predict it. A reason for this is the increasingly clear role of the ocean, especially that of the "Atlantic layer", on sea ice processes. We here quantify biases in that Atlantic layer and the Arctic Ocean deeper layers in 14 representative models that participated in the Climate Model Intercomparison Project phase 6. Compared to observational climatologies and hydrographic profiles, the modelled Atlantic layer core is too cold by on average -0.4°C and too deep by 400 m in the Nansen basin. The Atlantic layer is too thick, extending to the seafloor in some models. Deep and bottom waters are in contrast too warm by 1.1 and 1.2°C. Furthermore, the modelled properties hardly change throughout the Arctic. We attribute these biases to an inaccurate representation of shelf processes: only three models seem to produce dense water overflows, at too few locations, and these do not sink deep enough. No model compensates with open ocean deep convection. Therefore, the properties are set by the inaccurate fluxes through Fram Strait, biased low by up to 6 Sv, but coupled to a too-warm Fram Strait, resulting in a somewhat accurate heat inflow. These fluxes are related to biases in the Nordic Seas, themselves previously attributed to inaccurate sea ice extent and atmospheric modes of variability, thus highlighting the need for overall improvements in the different model components and their coupling.

SIGNIFICANCE STATEMENT: Coupled climate models are routinely used for climate change projection and adaptation, but they are only as good as the data used to create them. And in the deep Arctic, those data are few. We determine how biased 14 of the most recent models are regarding the deep Arctic Ocean and the Arctic's only deep gateway, Fram Strait (between Greenland and Svalbard). These models are very biased: too cold where they should be warm, too warm where they should be cold, not stratified enough, not in contact with the surface as they should, moving the wrong way around the Arctic, etc. Some problems also seem to come from out of the Arctic and/or from the sea ice models.

1. Introduction

The Arctic is one of the regions most affected by ongoing climate change (IPCC 2019), warming 2–3 times as fast as the global average (IPCC 2021) and consequently losing its sea ice cover. Since the beginning of the satellite record, the sea ice extent has been reduced by 9% in winter and 48% in summer (Docquier and Koenigk 2021), while the sea ice thickness has been reduced by 66% (Kwok 2018). The multi-year ice area has halved (Kwok 2018), and as a result the shelf regions have become seasonally ice free (Onarheim et al. 2018). These changes directly impact the upper Arctic Ocean, notably its freshwater content (Solomon et al. 2021, and references therein). Sea ice changes also seem to be caused by and to enhance changes in the deeper layers (Årthun and Eldevik 2016), in particular the Atlantic Water, via a process known as the "Atlantification" of the Arctic Ocean (Polyakov et al. 2017): The Atlantic Water is warmer, further into the Arctic, which reduces the sea ice cover, either by directly melting the ice or inhibiting sea ice growth, which in turn allows the atmosphere to modify water properties at greater depths. Climate models, however, fail to reproduce the sea ice evolution (Notz and SIMIP Community 2020), notably because their upper Arctic Ocean representation strongly varies among models (Ilıcak et al. 2016; Lique and Thomas 2018; Zanowski et al. 2021). We here investigate their representation of the deeper Arctic Ocean layers, from the Atlantic Water to the seafloor.

The Arctic Ocean consists of four deep basins (Fig. 1): the Nansen and Amundsen basins on the Eurasian side, and the Makarov and Canada basins on the Amerasian side, separated by the Lomonosov Ridge. The Eurasian basin contains two water masses below 1000 m (Smethie et al. 1988): the Eurasian Basin Deep Water (EBDW, down to 2500 m depth) and Eurasian Basin Bottom

Water (EBBW, from 2500 m to the seafloor). The denser deep and bottom waters are primarily the result of sea ice formation on the Siberian shelf (Nansen, F. 1906): when sea ice forms, brine is rejected, and the resulting dense water cascades off the shelf through troughs and canyons (Aagaard 1981; Rudels et al. 1999). This cascading is often referred to as "overflow", the term we use in this manuscript. The only deep connection between the Arctic Ocean and the global oceanic circulation is via Fram Strait (ca 2500 m deep), through which the comparatively warm and salty Atlantic Water enters from the Nordic Seas. After entering through Fram Strait, the Atlantic Water circulates cyclonically around the entire Arctic Ocean, its upper limit gradually deepening from the surface to ca 200 m depth, its lower limit never exceeding 1000 m (Rudels et al. 1999; Aksenov et al. 2011). However, its properties impact the whole water column as it can be entrained by the overflows (Smethie et al. 1988; Frank et al. 1998; Valk et al. 2020). At the bottom of Fram Strait, the EBDW flows out. Part of it mixes with fresh Greenland Sea deep waters and flows back into the Arctic through Fram Strait (Frank et al. 1998; Langehaug and Falck 2012; von Appen et al. 2015), below the Atlantic Water (Fig. 1). In the Amerasian basin, the deep water mass is the Canada Basin Deep Water (CBDW), the saltiest and warmest of the Arctic deep waters (Aagaard et al. 1985), suspected to be modified EBDW that intruded through the Lomonosov Ridge. There is no agreement as to whether this intrusion happens continuously (Timmermans and Garrett 2006), in pulses (Timmermans et al. 2005), or whether it happened and stopped centuries ago (Schlosser et al. 1997). The higher salinity and temperature of this CBDW compared to its Eurasian source is most likely caused by shelf overflows in the Amerasian basin (Rudels 1986; Ivanov et al. 2004). Eventually, CBDW intrudes back into the Eurasian basin through canyons in the Lomonosov Ridge (orange arrows on Fig. 1), as a very salty deep water mass (Björk et al. 2018).

To properly represent the deep Arctic circulation and water mass properties, models need to accurately simulate

- the interactions with sea ice and upper Arctic Ocean processes, especially ventilation and shelf processes;
- the large scale circulation within the Arctic, including bathymetry and mixing;
- Fram Strait and upstream ocean properties.

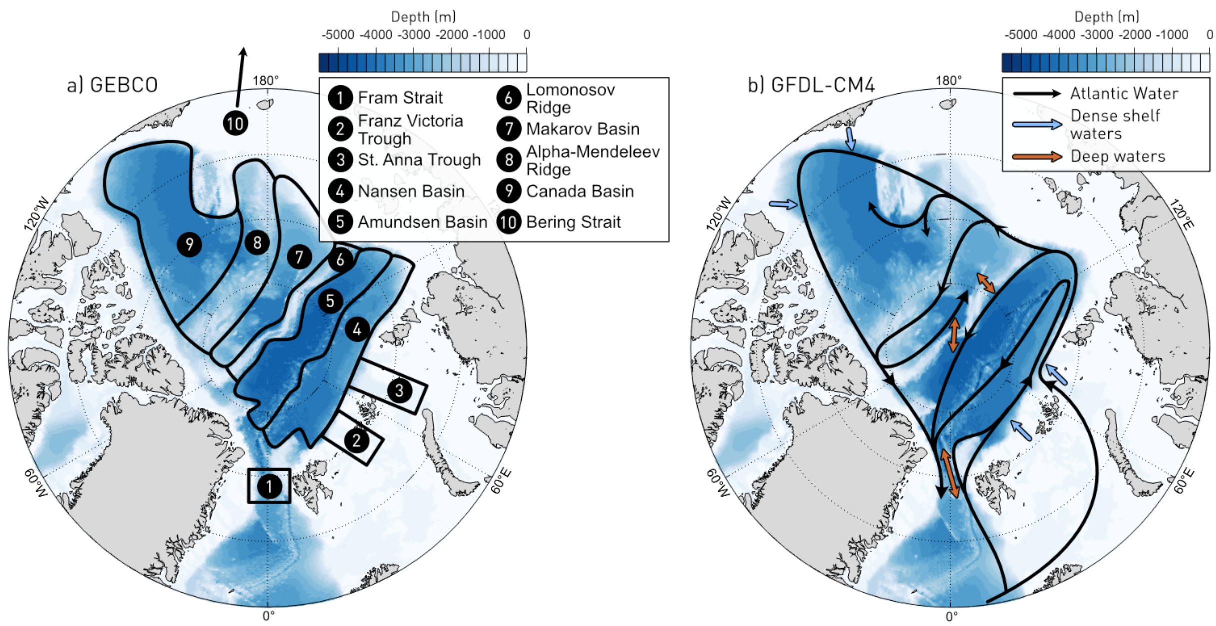

Fig. 1. Bathymetry of the Arctic north of 70 °N in a) GEBCO (GEBCO Compilation Group 2021) and b) the CMIP6 model with the highest horizontal resolution in our study (ca 9 km), GFDL-CM4 (Adcroft et al. 2019). Contours and numbers on a) highlight the regions discussed in this manuscript. Black arrows on b) indicate the known circulation of the Atlantic layer (e.g. Rudels 2009); blue arrows, some of the locations where dense shelf water is produced; orange arrows, the main features of the deep water circulation: Exchanges in and out of the Arctic through Fram Strait, and exchanges between the basins across the Lomonosov Ridge. This figure is a simplified, light schematic; the interested reader can find detailed circulation maps of all water masses in the review by Rudels (2012).

Earlier studies suggest that accurately simulating all these processes was challenging in the previous generation of climate models (Shu et al. 2019) and will continue to be challenging for the models that participated in the latest Climate Model Intercomparison Project, phase 6 (CMIP6, Eyring et al. 2016): their Arctic sea ice (Notz and SIMIP Community 2020), Arctic solid and liquid freshwater storage and fluxes (Zanowski et al. 2021; Rosenblum et al. 2021), and properties and processes upstream in the Nordic Seas (Heuzé 2021) are inaccurate, or at least the models have a large range of behaviours. The vast majority also fail to reproduce overflows in other parts of the world (Adcroft et al. 2019; Heuzé 2021). Although not directly resolved in climate models, various turbulent mixing processes (including tides, the generation of internal waves, and eddies) are known to influence the hydrographic structure of the Arctic Ocean (Rippeth and Fine 2022). Despite the levels of turbulent kinetic energy generally being much lower in the Arctic Ocean than elsewhere across the global ocean (Pinkel 2005; von Appen et al. 2022), mixing contributes to stirring up heat from intermediate depths (Polyakov et al. 2020) and stirring down freshwater (Manucharyan and Spall 2016), hence influencing the stratification. Generally, wind-induced mixing is limited in the Arctic, partly due to the decoupling of the ocean from the atmosphere by sea ice (Morison et al. 1985), but mixing due to tides has been shown to be an important process, especially on the shelves and near the shelf break where they generate internal waves (Rippeth et al. 2015; Fer et al. 2020). Eddies can intensify vertical mixing (Rippeth and Fine 2022, and references therein), but also play an important role in the transport of water masses between the shelves and the deep basins (Spall et al. 2008). The parametrizations of such processes are thus likely to be of importance for the representation of the deep water masses of the Arctic Ocean.

Khosravi et al. (2022) recently published an overview of biases in the Atlantic Water in CMIP6 models; we here expand on their results by assessing not only the Atlantic Water but also the deep and bottom waters, and by explaining the causes for all these biases, focussing on the models' mean historical state only. We start by describing the 14 CMIP6 models and methods that we use (Section 2) before quantifying the biases in all Arctic deep waters in all basins (Section 3a). We then assess the representation of overflows (Section 3b) and circulation of the deep water masses within the Arctic (Section 3c) and finally evaluate the fluxes through Fram Strait and their relation to the biases in the Arctic (Section 3d). We finish with a discussion, notably on possible directions for CMIP7 (Section 4).

2. Data and Methods

a. The CMIP6 models

We use the output from 14 fully coupled models that participated in the Climate Model Intercomparison Project phase 6 (CMIP6, Eyring et al. 2016), listed in Table 1. These models were selected, following a preliminary study on the 35 CMIP6 models used in Heuzé (2021), as representative of their family, for diversity in vertical grid types, for comparison with those used in a companion paper (Muilwijk et al. subm.), and after eliminating the ones with the poorest bathymetry (i.e absence of Lomonosov Ridge and/or unrealistically narrow Fram Strait). Most of the models we selected have a resolution of ~50 km in the Arctic (9 km for the highest resolution) and 50 levels

TABLE 1. Characteristics of the 14 CMIP6 models used in this study: horizontal grid type, which output if any are missing, horizontal resolution in the Arctic, type of vertical grid and number of vertical levels, ocean model component, vertical mixing scheme(s), ocean climatology used to initialise the model, and reference. The horizontal resolution in the Arctic (4th column) was calculated as the square root of the total area north of 70°N divided by the number of points the model has north of 70°N. For the vertical grids, ρ means isopycnic; σ terrain-following; and several symbols, hybrid. For the vertical mixing schemes, we use a similar nomenclature to that of Huang et al. (2014) for CMIP5: KPP = K-profile parameterization scheme (Large et al. 1994), TM = tidal mixing parameterization, ePBL = energetics-based planetary boundary layer (Reichl and Hallberg 2018), NK = Noh and Jin Kim (1999), PP = Pacanowski and Philander (1981), DL = Decloedt and Luther (2010), TC = turbulent closure scheme, and K90 = Kraus (1990).

Model	Grid type	Missing	Hor. Res.	Vert. grid	Ocean model	Vert. mixing	Init.	Reference
BCC-CSM2-MR	Tripolar	agessc	54 km	z/40	MOM4-L40v2	KPP	WOA13	Wu et al. (2019)
CAMS-CSM1-0	Tripolar	agessc	54 km	z/50	MOM4	KPP	WOA2001	Rong et al. (2019)
CESM2	Rotated	/	41 km	z/60	POP2	KPP	PHC2	Danabasoglu et al. (2020)
CanESM5	Tripolar	/	50 km	z/45	NEMO3.4.1	TM	WOA09	Swart et al. (2019)
EC-Earth3	Tripolar	agessc	49 km	z*/75	NEMO3.6	TC	WOA13	Döscher et al. (2021)
GFDL-CM4	Tripolar	agessc	9 km	ρ-z*/75	MOM6	ePBL	WOA13	Adcroft et al. (2019)
GFDL-ESM4	Tripolar	agessc, uo, vo	18 km	ρ-z*/75	MOM6	ePBL	WOA13	Dunne et al. (2020)
GISS-E2-1-H	Regular	agessc	46 km	ρ-z-σ/32	Hycom	KPP	WOA13	Kelley et al. (2020)
IPSL-CM6A-LR	Tripolar	/	49 km	z*/75	NEMO3.2	TC	WOA13	Boucher et al. (2020)
MIROC6	Tripolar	/	39 km	z-σ/62	COCO4.9	NK	PHC3	Tatebe et al. (2019)
MPI-ESM1-2-HR	Tripolar	/	36 km	z/40	MPIOM1.63	PP	PHC3	Müller et al. (2018)
MRI-ESM2-0	Tripolar	/	39 km	z*/60	MRI.COMv4	DL	WOA13	Yukimoto et al. (2019)
NorESM2-LM	Tripolar	/	38 km	ρ-z/53	BLOM (MICOM)	TC	PHC3	Seland et al. (2020)
UKESM1-0-LL	Tripolar	/	50 km	z*/75	NEMO3.6	K90	EN4	Sellar et al. (2019)

or more in the vertical. No more than two models share the same ocean component with the same version, and these 14 models have been initialised using 6 different ocean climatologies (Table 1).

The 14 models include a wide variety of mixing schemes, from a simple linear increase of vertical diffusivity with depth to more complex kinetic energy closure schemes. It is worth noting that the information presented in Table 1 is probably incomplete as the model descriptions are inconsistent both in wording and level of detail. Interestingly, several of the most extensive references list modifications relevant for the Arctic and/or for overflows (quoted from the cited papers):

- EC-Earth3 has a "diffusive bottom boundary layer scheme with implicit bottom friction to mix dense water down a slope" (Döscher et al. 2021);
- GFDL-CM4 includes an overflow parameterization in the Nordic Seas, but not yet in the Arctic (Adcroft et al. 2019);
- in MIROC6, "the turbulent mixing process in the surface mixed layer is changed so that there is no surface wave breaking and no resultant near-surface mixing in regions covered by sea ice", which the authors argue "contributes to better representations of the surface stratification in the Arctic Ocean" (Tatebe et al. 2019);
- in NorESM2-LM, "selective damping of external inertia–gravity waves in shallow regions is enabled to mitigate an issue with unphysical oceanic variability in high-latitude shelf regions that had caused excessive sea-ice formation in CMIP5" (Seland et al. 2020);
- finally in UKESM1-0-LL, the albedo of snow on sea ice is decreased as "compensation for deficient transport of warm Atlantic water into the Arctic in ORCA1" (Sellar et al. 2019).

We evaluate the last 30 years of the historical run, i.e. January 1985 - December 2014. We use only one ensemble member for each model, labelled 'r1i1p1f1', except for UKESM1-0-LL for which we use 'r1i1p1f2' as r1i1p1f1 was not available. The output we use are the monthly seawater salinity 'so', potential temperature 'thetao', eastward velocity 'uo', and northward velocity 'vo', except for GFDL-ESM4 for which uo and vo were not archived. We also use the sea ice concentration 'siconc' and sea ice thickness 'sivol' (in fact, sea ice volume divided by grid cell area; available for a majority of models), except for CanESM2 for which we use 'sithick' as 'sivol' was not available (actual floe thickness; available for few models). For 8 models, we also use the seawater age since surface contact 'agescc', which we will hereafter refer to as the age of water. For the mixed layer depth, we use the 'mlotst' output when available, and otherwise computed it as per the CMIP6 protocol by first computing the potential density σ_θ from the monthly salinity and temperature, and then using a threshold of 0.125 kg m^{-3} referenced to 10 m depth. The 'mlotst' and computed values are not the same due to the non-linearity of the equation of state, but as shown in Heuzé (2021), the difference is not significant for shallow mixed layers. With the exception of the mixed layer and flux computations, we use the density referenced to 2000 m depth (σ_2) as a compromise considering the wide range of depths covered. The diagnostics based on σ_2 differences were also done using σ_0 and σ_4 (not shown), but no significant differences in any of our results were found. All densities were computed using the TEOS10 equation of state as implemented in the Gibbs-SeaWater (GSW) Oceanographic Toolbox (McDougall and Barker 2011).

All computations were performed on the models' native grid with these two exceptions:

- The GISS-E2-1-H and NorESM2-LM native vertical grids were particularly challenging to work with, so we instead show their regularised grid output. We nevertheless verified that our key results still hold on the native grid;
- The comparisons to the climatology in section 3.a and 3.d were performed after interpolating all the model temperature and salinity values onto the WOA18 (see next section) climatology's grid.

b. Observational data

To quantify biases in the CMIP6 models, we first compare them to the Unified Database for Arctic and Subarctic Hydrography (UDASH, Behrendt et al. 2018) by generating basin- 30-year-average temperature and salinity profiles in the four deep basins of the Arctic Ocean (as defined on Fig. 1). As the UDASH profiles are scattered, rather than interpolating them ourselves we use the World Ocean Atlas 2018 (WOA18, Locarnini et al. 2018; Zweng et al. 2018) objectively analysed annual fields at a 0.25° resolution (ca 25 km) for all computations where the model and observations had to be colocated.

Most models use an earlier version of the World Ocean Atlas as initialisation (Table 1), with 7 out of 14 models using the version that was the latest as the models ran, i.e. WOA13. Two models use an even earlier version from 2009 or even 2001. The main difference between the versions is the amount of data ingested and the time period of the data; the reader will find more information about the versions' differences in the WOA18 publications (Locarnini et al. 2018; Zweng et al. 2018). The second most common climatology is the Polar science center Hydrographic Climatology (PHC, Steele et al. 2001), which includes the WOA98 data and the Arctic Ocean Atlas (AOA, Environmental Working Group 1997, 1998), gridded compilation of previously classified US and Russian hydrographic data collected during the Cold War; the one disadvantage of PHC is that the latest version, PHC3, was last updated in 2005. Finally, one model uses the Met Office Hadley

Centre climatology EN4 (Good et al. 2013), which merges the World Ocean Database 2009 with autonomous data (see Good et al. 2013, for more information); in the ice-covered regions, these are to date limited to the upper 1000 m (see review in Rabe et al. 2022). For robustness, we computed the model biases relative to all these datasets as well and found no significant difference in our results, most likely because the number of profiles in the deep Arctic remains extremely low to this day, therefore differences between the observational datasets are negligible compared to the model biases. We therefore keep the higher spatial resolution WOA18 as our reference, as it also is the most directly comparable to UDASH.

c. Methods

The primary objective of this paper is to quantify biases in the properties of the deep water masses of the Arctic Ocean: the Atlantic Water (AW), the Eurasian Basin Deep Water (EBDW), its counterpart the Canada Basin Deep Water (CBDW), and the Eurasian Basin Bottom Water (EBBW). Traditionally, for observational datasets, the definition of these water masses is based on temperature, salinity, or density values (e.g. Smethie et al. 1988; Rudels 2009; Korhonen et al. 2013). As we expect these properties to be biased in the models, we instead chose these three definitions:

- the Atlantic Water core is the depth of the temperature maximum, detected between 150 and 2000 m depth. This temperature-based definition is similar to that used for observations, but without imposing a constraint on the value of the temperature maximum, and adjusted for the wider depth range in models. Note that using a threshold of 100 m instead of 150 m does not change the results, probably because as found by Lavoie et al. (2022), Pacific Water tends to be missing from CMIP models, a result not surprising given their biases in Bering Strait inflow (Zanowski et al. 2021);

- deep water properties are those at 2000 m. In observations, EBDW sits between approx. 1000 and 2500 m depth in the Eurasian basin, and CBDW extends from approx. 1000 m all the way to the seafloor;

- bottom water properties are those of the deepest grid cell with a value.

The upper ocean is not the topic of this paper. We nevertheless investigate whether biases in the upper ocean and in the deep layers are related, and therefore computed the mean temperature, salinity, and density in the top 100 m as a proxy for upper ocean properties. Similarly, a detailed study of stratification is provided by Muilwijk et al. (subm.); we here only provide a simplified definition of stratification, taken as the difference between the upper 100 m mean density and that of the AW core.

We compare the properties of the different water masses in the four deep basins of the Arctic north of 70°N (Fig. 1a), where "deep" is defined as deeper than 2000 m. The shelf is defined as regions shallower than 1000 m (Rudels 2009). Note that the 1000 m and 2000 m isobaths coincide at most locations in most models, as the shelf break is very steep. Throughout this manuscript, we use the short name "Siberian shelf" to refer to the shelf along the Eurasian basin, i.e. from Fram Strait to 160°W. As we will show, no deep water formation occurs on the shelf along the Canada basin in CMIP6 models, so we do not focus on this region. Finally, to investigate the deep outflows from the Arctic, we determine the biases on the Greenland shelf, i.e. around Greenland but north of 70°N.

In the Arctic, dense waters cascading from the shelf to the deep basin, commonly referred to as overflows, strongly modify the properties of all water masses (e.g. Aagaard 1981; Luneva et al. 2020). As summarised in Luneva et al. (2020), these overflows are bottom-trapped gravity currents characterised by a comparatively high density, but also by a young age, as dense shelf waters sink off the shelf within the same year that they sank from the surface to the shelf seafloor. Therefore, we detect their presence in models by studying:

- the minimum age at the bottom grid cell, for the 8 models that provided the age of water output
- the maximum bottom density, for the other 6 models.

For both groups of models, we look for a continuity in this diagnostic on and off the shelf, in maps of the bottom properties, and in sections along and across the troughs where we expect their presence.

Finally, we determine the influence of Fram Strait on the deep Arctic Ocean properties by computing the volume, salt, and heat fluxes through that section, from the surface to the sea floor, as follows, where S is the salinity, θ is the potential temperature, ρ is the *in situ* density (computed using TEOS10 when necessary), and c_p the specific heat at constant pressure:

$$F_{volume} = \iint_A \mathbf{v} \cdot \hat{n} dA \tag{1}$$

$$F_{salt} = \iint_A S\mathbf{v} \cdot \hat{n} dA \tag{2}$$

$$F_{heat} = c_p \iint_A \rho\theta\mathbf{v} \cdot \hat{n} dA \tag{3}$$

For the models used here c_p ranges from 3990-4000 J kg^{-1} K^{-1}. Following Griffies et al. (2016), for Boussinesq models the reference density, ρ_0, is used to compute the heat flux and ranges from 1000-1036 kg m^{-3}. Note that strictly speaking, this is not the true transport as this would require a closed volume budget across Fram Strait (Schauer and Beszczynska-Möller 2009). This method is nevertheless routinely used to compute "volume fluxes" and "heat fluxes" from observations, so we use it to enable comparison between models and the observed Arctic and refer to these computed values as fluxes (without quotation marks). Besides, each model's heat flux should in theory be computed relative to a temperature representative of the flow. That is, for each model, the shallow inflow, shallow outflow, deep inflow and deep outflow, if all clearly distinguishable, would each have a different reference temperature. To ease the across-model comparison, all heat fluxes are instead computed relative to 0°C (as done in e.g. Ilıcak et al. 2016; Muilwijk et al. 2018). Similarly, instead of computing a so-called freshwater flux, i.e. relative to a reference salinity which would, again, have to be meaningful for each specific model, we compute the flux of salt. As its value is rarely given in the literature, we focus our analysis on F_{volume} and F_{heat}.

As in Zanowski et al. (2021), the boundaries for Fram Strait were chosen by hand for each model and span 20°W-12°E, 78°N-80°N. The results are not sensitive to the choice of exact boundaries within that range, but should ideally be as close to 79°N as possible for comparison with observations (e.g. Beszczynska-Möller et al. 2012). For the rotated and tripolar grids, the northward velocity 'vo' does not correspond to velocities towards the true north 90°N but rather towards the model's location of the North Pole. Therefore, for all models, $\mathbf{v} \cdot \hat{n}$ is the velocity into / out of the Arctic, normal to the model's coast-to-coast section. All fluxes were computed on the models' native horizontal grids (shown on supp. Fig. A1). CMIP6 variable 'thkcello' (ocean model cell thickness) was used for those models with time-varying cell thicknesses, unless specific instructions were provided in the model output for computing cell thickness (i.e., MIROC6, GFDL-CM4).

3. Results

In this section, we first quantify the biases in the properties of the Atlantic Water, deep, and bottom water masses and their horizontal and vertical relationships. We then evaluate the representation of the processes that set these properties, within the Arctic Ocean (subsections 3b and 3c) and at Fram Strait (subsection 3d).

a. Biases in water mass properties

We start by quantifying biases in the mean temperature and salinity and their evolution with depth in the four deep basins (Fig. 2 and individual values in supp. Tables A1 to A3). In observations, as the Nansen basin lies closest to its inflow, the Atlantic Water there is warm (black line, Fig. 2a), salty (Fig. 2b) and constrained to a thin and shallow depth range, around 200 m depth. In the models in contrast, the Atlantic Water lies deeper (multimodel average of 395 m, ranging from 76 to 1321 m) and occupies a thicker layer, which is in agreement with the findings of Khosravi et al. (2022) in CMIP6, and Ilıcak et al. (2016) for CORE-II. In fact, had we used the standard definitions that the Atlantic Water is anything warmer than 0°C (e.g. Korhonen et al. 2013) or lighter than 27.97 kg m^{-3} (e.g. Rudels 2009) (black dotted lines on Fig. 2c), we would have found Atlantic Water all the way to the seafloor in half of the models. Therefore, although on average the models are biased cold in the Atlantic Water core (multi-model mean of -0.44°C), they are biased warm at 2000 m depth (MMM of 1.14°C) and at the bottom of the Nansen basin (1.25°C). The salinity profile is also inaccurate: when in observations the salinity is maximum in the AW core, in 10/14 models the salinity continues to increase with depth. Consequently, the T-S diagram in the Nansen basin (Fig. 2c) is unrealistic for the majority of the models. Most models have a shape somewhat resembling that of the observations (black), but with peaks at the wrong temperature and/or salinity and of a largely inaccurate magnitude (see e.g. CanESM5, plain blue line). The least inaccurate is GFDL-CM4 (plain green line), despite an AW core lying on average 400 m too deep and the whole AW layer extending to 2000 m depth. One of the most inaccurate is NorESM2-LM, which has many discontinuities in its hydrographic profiles. This is because on its native isopycnic grid

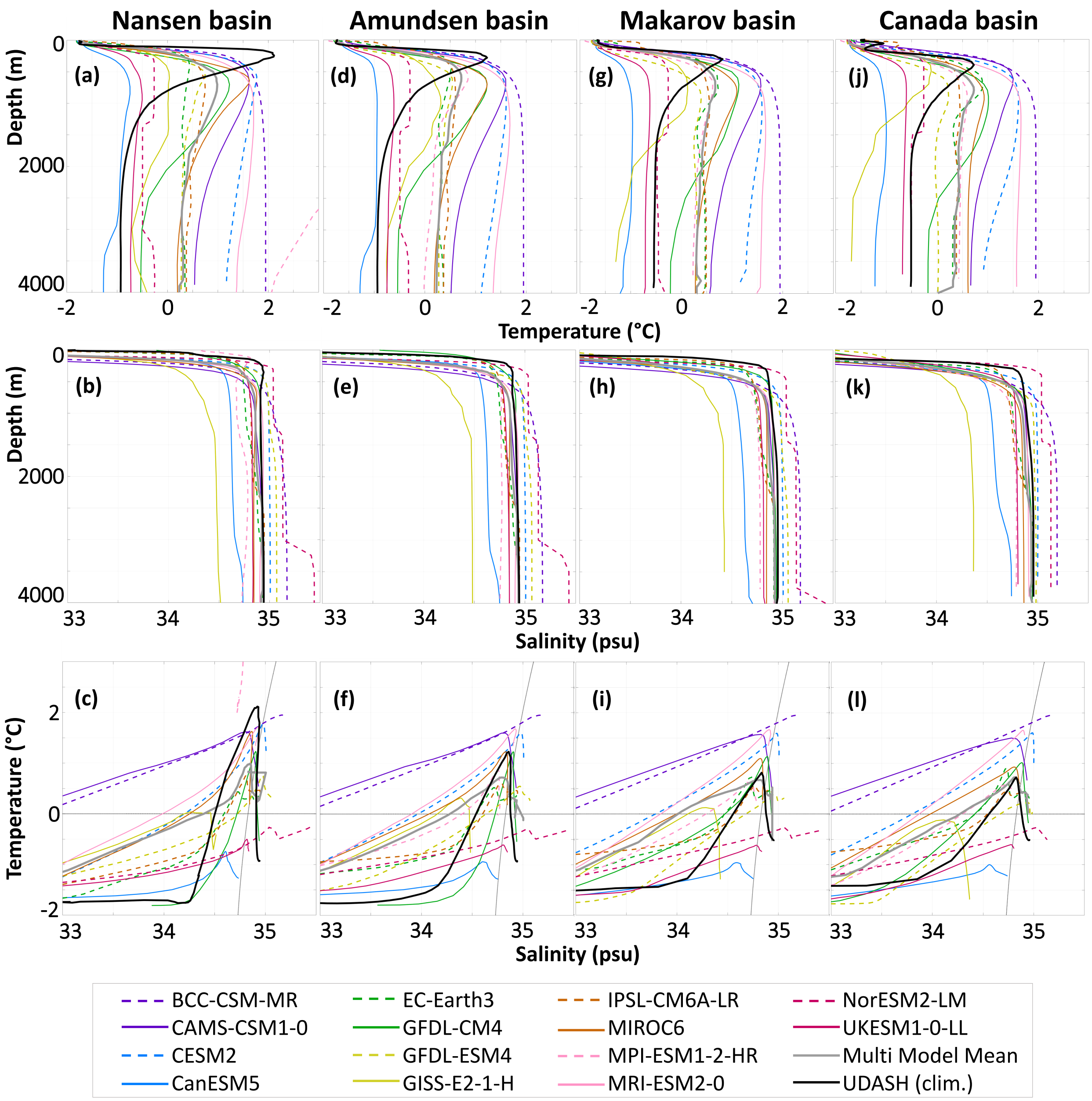

FIG. 2. Area-weighted mean temperature (top) and salinity (middle) profiles with depth, and corresponding T-S diagram (bottom), for each CMIP6 model (colours), the multimodel mean (gray) and the observations in UDASH (black, Behrendt et al. 2018), for each of the deep Arctic basins. MPI-ESM1-2-HR is not visible on panel a) as its temperature is biased too warm (over 10°C in the upper ocean). On the T-S diagrams, the black dotted lines indicate the 0°C isotherm and 27.97 kg m^{-3} isopycnal.

(not shown), as the model is comparatively unstratified, some density classes occupy hundreds of metres. On average, the models are less stratified than observations: they have a dense bias in the AW and a light bias in the deeper layers; this result will be important in subsection 3b when investigating the ventilation.

All four deep basins exhibit the same biases: the Atlantic layer is too deep, too thick, and in some cases occupies the entire depth of the basin (Fig. 2). This suggests that the biases throughout the water column are linked (Fig. 3). To verify this link, we compute the across-model correlation, i.e. each model is represented by its 30-year average, basin-average value, and the correlation between models is tested. For all basins, the across-model relationship between any two properties of the different water masses in that basin is split in two distinct depth levels:

- The biases in the upper 100 m are strongly correlated to each other: warm biases are associated with salty biases, which are associated with dense biases, and in turn with a weak stratification. These upper ocean biases are further investigated in Muilwijk et al. (subm.) and beyond the scope of this paper. What is relevant for this study is that the biases in the upper 100 m are not correlated to those of the deeper water masses (empty squares in the top four lines, Fig. 3).

- From the Atlantic layer down, the biases in all properties and water masses are positively correlated to each other. As our definitions artificially split the Canada Basin Deep Water in two different water masses (2000 m depth and bottom), we expect a strong correlation between these two depth levels in the Makarov and Canada basins. However, the correlations are larger than 0.9 across all basins and depth levels (diagonal of deep red values, Fig. 3), and the actual values nearly align along the unit line when plotted against each other (not shown). As suspected from Fig. 2, most models in our study do not have distinct deep water masses, but rather fill the deep basins with a similar water from the Atlantic Water level to the seafloor.

Note that Fig. 3 was created using the area-weighted means, but the same results were found if using the area-weighted root mean squared error (RMSE) or the actual properties. Finally, the reader may have noticed that the Atlantic Water core depth (AWCD) is not correlated to any other property – we will come back to this finding later in the manuscript.

In observations, the properties of each water mass evolve not only with depth but also horizontally. Most visibly, the Atlantic Water becomes colder, fresher, deeper and thicker, and consequently results in a less pronounced peak on the T-S diagram as it travels from the Nansen basin to the Canada basin (black lines, Fig. 2). We do not observe this in models. AW density and temperature show little change across the Arctic. As a result, the biases (supp. Tables A1 to A3) change primarily because the value in the reference climatology changes rather than the values in the models. This is most visible when the properties are mapped (Fig. 4 and supp. Figs. A2 and A3): the AW appears biased dense and cold the most in the Nansen basin, as it is the basin where the density is lowest and temperature highest in the climatology. The maps reveal that no basin is better represented than the others; rather, the difference is largest when comparing the different water masses (RMSE value on Fig. 4), and when comparing the deep basins to the shelves. No model clearly outperforms the others; the model that can be qualified of "most accurate" depends on the depth and property considered (Fig. 4 and supp. Figs. A2 and A3, second row).

As for the evolution with depth, we verify that for each water mass its biases are consistent throughout the Arctic as suggested by Fig. 4 by computing the across model correlations between the basins (Fig. 5). For the four deep basins, the temperature and the salinity, and the three water masses, the correlations often exceed 0.9 (dark red on Fig. 5). There are two exceptions:

- On the Siberian shelf, there are no correlations with the deep basins. This suggests that the majority of models do not accurately represent the connection between the Siberian shelf and the deep basin via dense water overflows. We investigate this further in the next subsection.
- On the Greenland shelf, there are no significant correlations in salinity but strong correlations in temperature, especially with the AW in the deep basins. This suggests that the flow of Atlantic Water from the deep basins southward and onto the Greenland shelf, notably through Fram Strait, may be accurately represented. We investigate this further in the next subsections.

In summary, across CMIP6 models, the Atlantic layer is biased cold, fresh, and dense when compared to observations, while the deep and bottom waters are biased warm, fresh, and light. The biases between water masses are strongly correlated to each other, and coupled with the fact that the AW occupies nearly the entire water column in most models, suggest that the different water masses are not significantly different from each other. The biases are also consistent throughout the Arctic. In the next two subsections, we investigate whether this lack of variation with depth and with distance is caused by inaccurate ventilation and circulation of these waters within the Arctic.

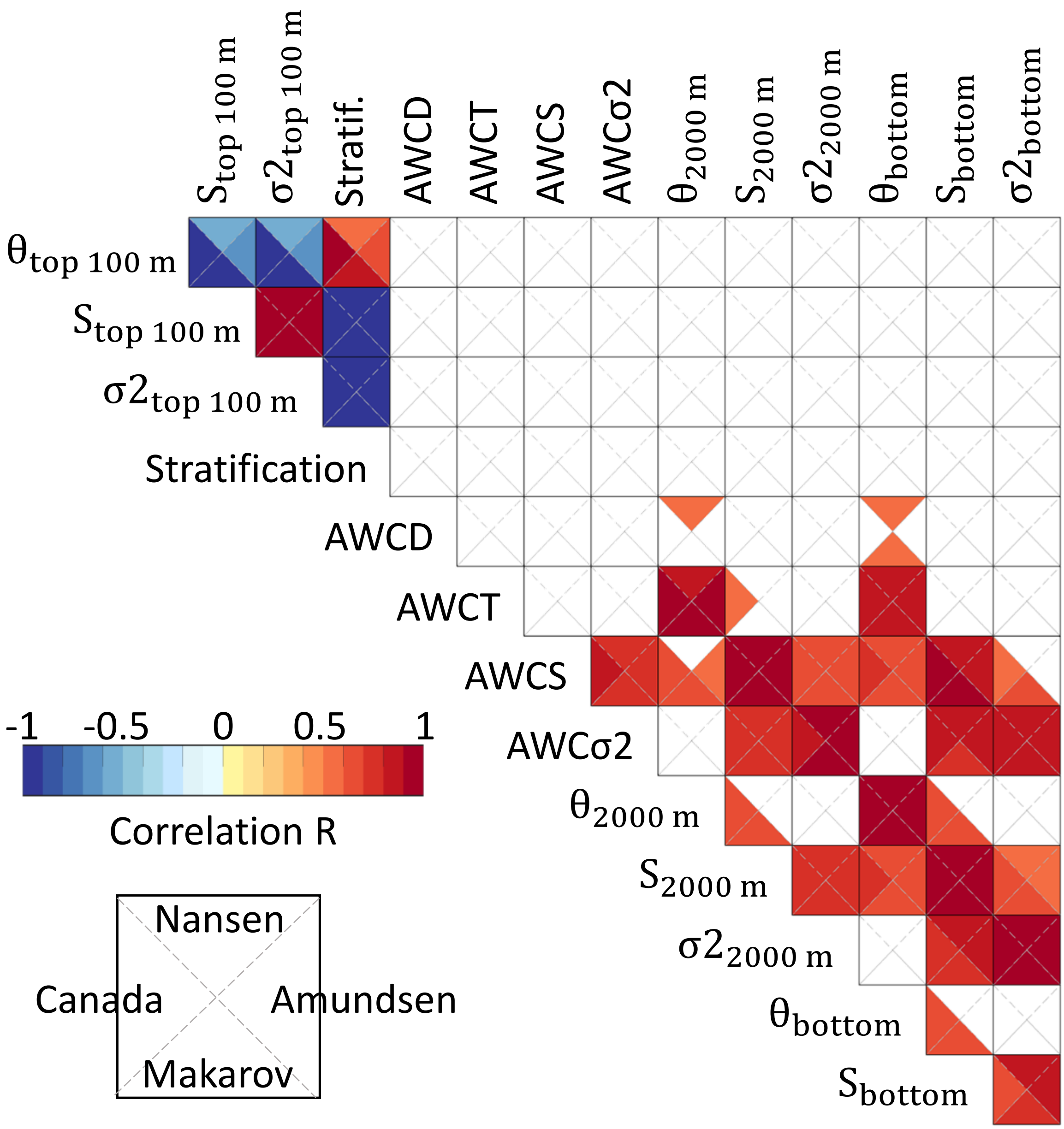

FIG. 3. Across-model correlation between the biases in water mass properties throughout the water column, for each deep basin (individual triangles): Mean temperature, salinity and density of the upper 100 m as proxies for the halocline; stratification, i.e. density difference between the halocline and the Atlantic Water core; Atlantic Water core depth (AWCD), temperature (AWCT), salinity (AWCS) and density (AWCσ2); temperature, salinity and density at 2000 m depth as proxies for the deep water; and temperature, salinity and density at the bottom. See methods for more information. Only correlations significant at 95% level shown (non-significant correlations are white).

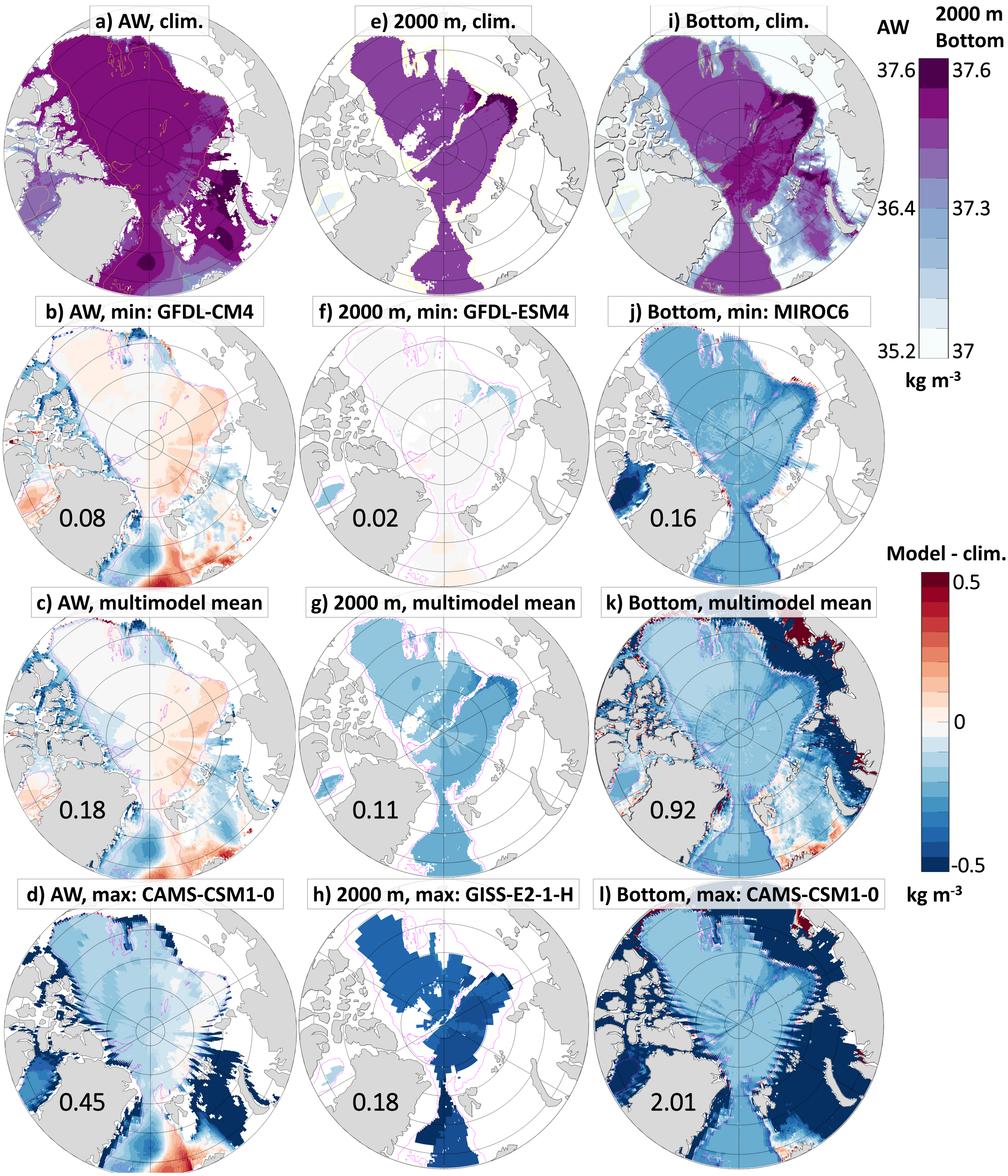

FIG. 4. Density σ_2 in the WOA18 climatology (top row) and bias when compared to this climatology for the least biased model (second row), the multimodel mean (third row) and the most biased model (last row), for the Atlantic Water core (first column), 2000 m depth (second column), and the bottom (last column). Yellow line on the top row, magenta otherwise, is the 2000 m isobath. The numbers are the respective Pan-Arctic area-weighted root mean square errors. See supp. Figs A2 and A3 for the temperature and salinity.

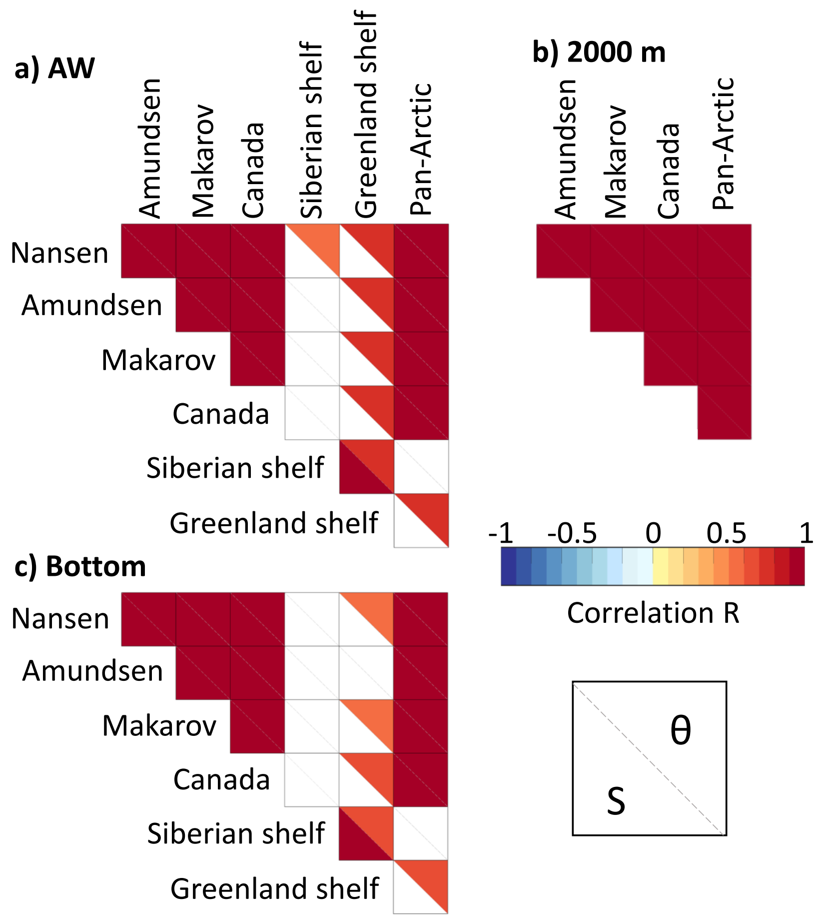

FIG. 5. Across-model correlation in the biases in each water mass temperature θ and salinity S between regions, for a) the Atlantic Water core, b) the deep water at 2000 m depth (no value on the shelves as per shelf definition), and c) the bottom. See methods for more information, in particular for the regions' definitions. Only correlations significant at 95% level shown.

b. Ventilation of deep water masses within the Arctic

We just showed that there is no across-model correlation between the Atlantic Water and deeper ocean biases and those in the upper ocean. This means that the deep biases may come from an inaccurate representation of the processes that normally form or modify those deep waters: ventilation within the Arctic; circulation within the Arctic; or exchanges through Fram Strait. We start with the processes that take place within the Arctic, and in particular with dense water overflows.

Of the 8/14 models that provided the age of water as a parameter, only two appear to simulate overflows at the Arctic shelf break (Fig. 6a and d, regions highlighted with green boxes): NorESM2-LM, through Franz-Victoria Trough and St Anna Trough; and MIROC6, through St Anna Trough only. For both these models, the overflow is visible as a continuous 0 to 1 year age on either side of the 1000 m isobath. We attempt to track these overflows as they travel off the shelf break, but both in animations (not shown) and in sections across (Fig. 6b and e) and along (c and f) the shelf break, we can only detect the occasional grid cell with a low age and not a clear flow. These suggest that NorESM2-LM may ventilate down to 3000 m depth occasionally, and MIROC6 to 2000 m. These two models also have the least biased deep and bottom waters for the entire Arctic (see previous section). One of the reasons for these models' relatively good performance may be their different vertical grids than the other 6 models in this subsample (isopycnic and terrain-following, respectively), which should be particularly well-suited to represent a density-driven flow along a slope (e.g. Dufour et al. 2017, and references therein).

For the remaining 6/14 models, we use bottom density as a proxy for ventilation. Only GFDL-ESM4 may have a dense water overflow, in St Anna Trough (Fig. 6g), but tracking its progression down the shelf (Fig. 6h,i) is not trivial. Referencing the density to different depth levels did not make the result clearer. As GFDL-ESM4 is the model that we previously found to have the least biased 2000 m salinity and density, it is possible that it has intermittent overflows. Besides, GFDL-ESM4 and NorESM2-LM are able to simulate overflows on the Antarctic shelf break (Heuzé 2021), which suggests the potential for them to do the same in the Arctic. Either way, previous studies have shown that overflows occur at several other locations, including at the Canadian shelf break (Luneva et al. 2020). Of the 14 models we study here, however, only 3 models show indications of simulating overflows, all in the same troughs.

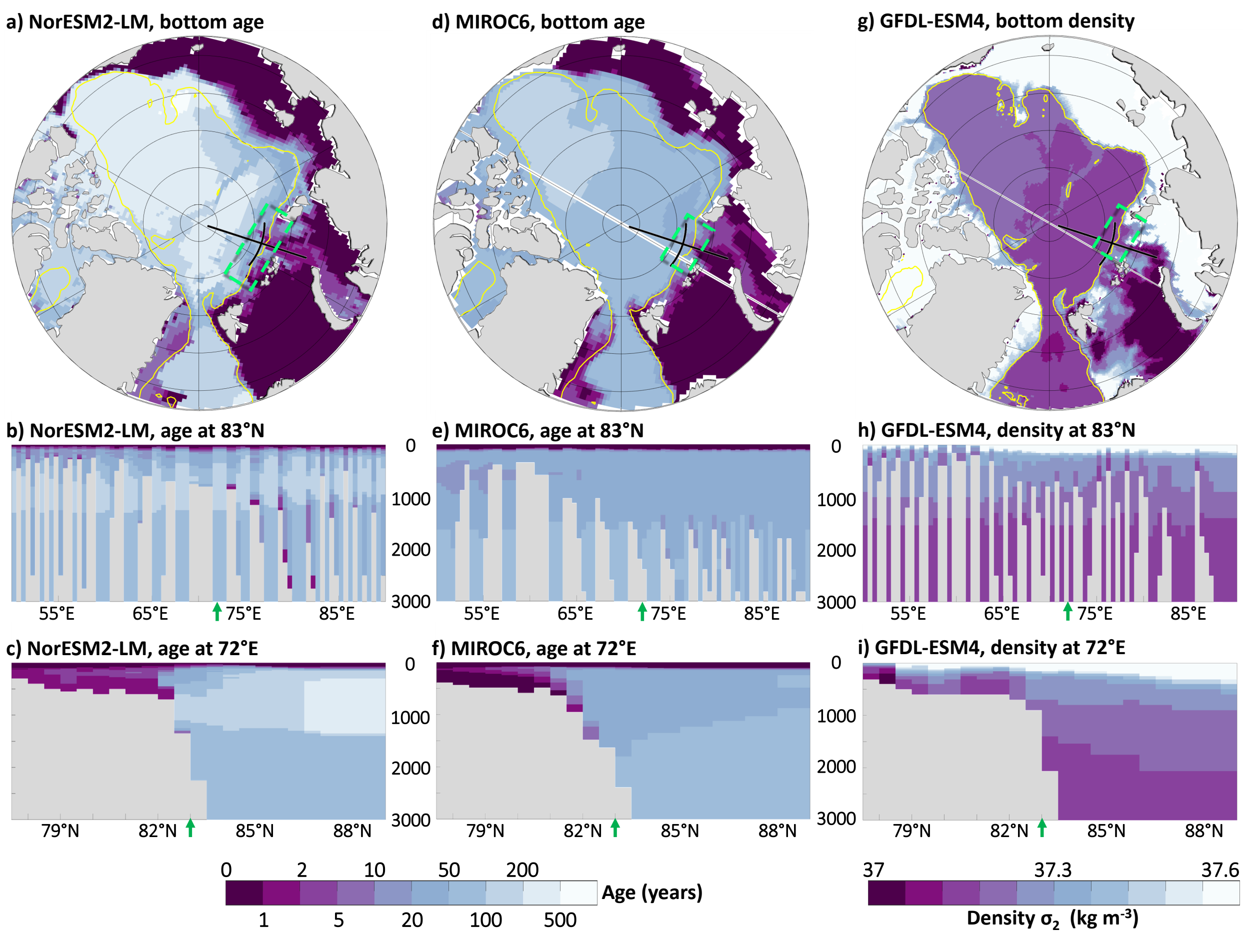

FIG. 6. For the three models that appear to have overflows, top: Map of the minimum age of water / maximum density σ_2 over the period 1985-2014 at the deepest grid cell (shading) and 1000 m isobath (yellow line), where a low age / high density on either side of this isobath suggests overflowing at the shelf break. Green boxes highlight the location of such overflow; black lines, the location of the sections on the other panels. Centre and bottom: Sections along (83°N) and across (72°E) St Anna Trough of the age of water / density σ_2. Note the logarithmic colour scale for the age.

Why are these three model the only ones with overflows, and why in St Anna Trough (SAT) only? Starting with the models' bathymetry (gray shading on Fig. 7), BCC-CSM-MR and CAMS-CSM1-0 do not even have a trough there; their bathymetry is shallower than 500 m on the entire continental shelf. For all the other models, SAT is the only trough represented. One possibility therefore is that the models form dense water elsewhere on the shelf, but cannot export it. In observations, dense water formation is caused by sea ice processes, in particular polynyas, with

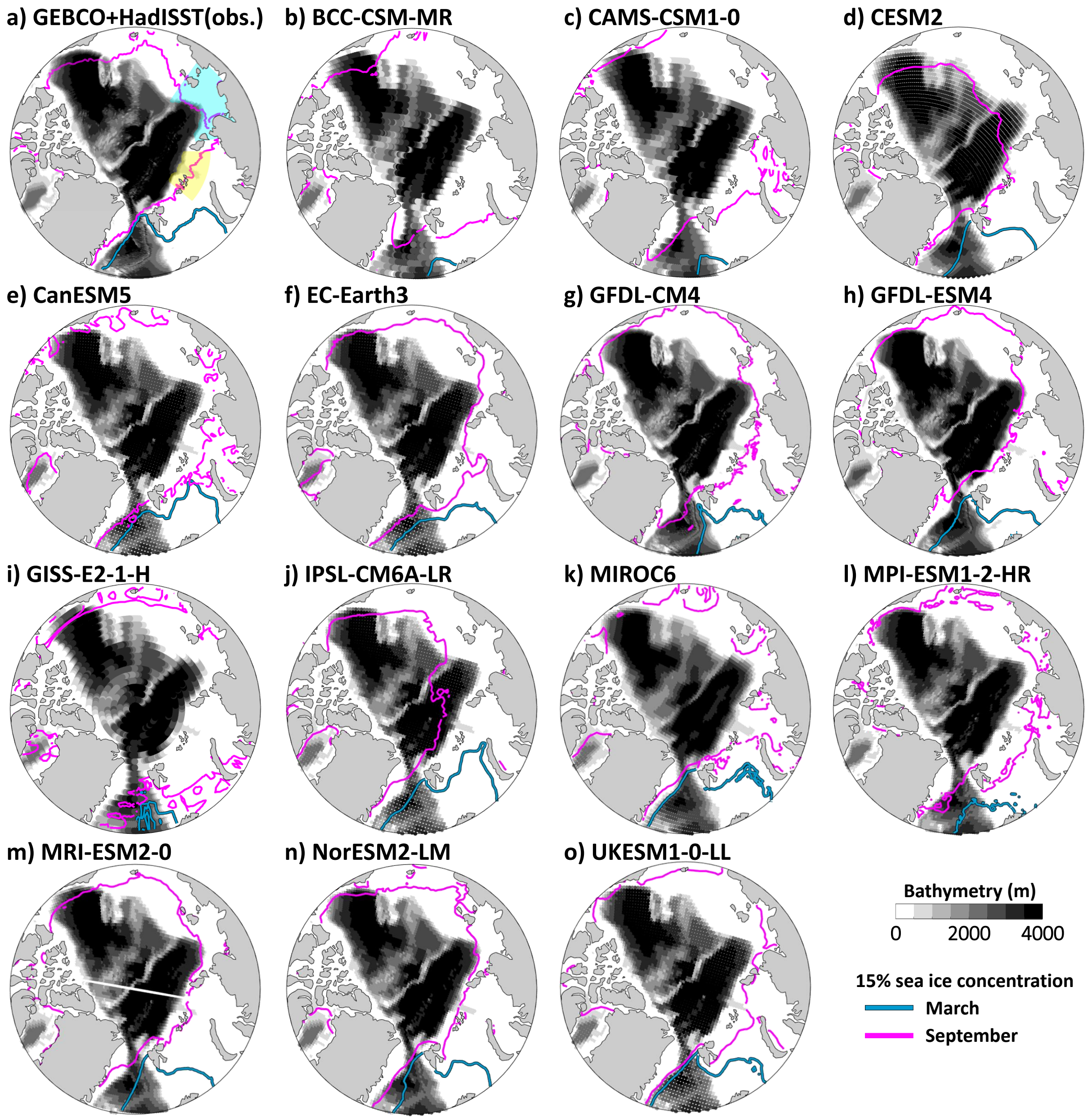

FIG. 7. Bathymetry (dark shading) and 30-year 1985-2014 mean March (blue) and September (magenta) sea ice extent for a) observations, here the GEBCO bathymetry (GEBCO Compilation Group 2021) and HadISST1 sea ice concentration (Rayner et al. 2003), and b)-o) the CMIP6 models, on their native grid. The yellow and cyan shaded areas on panel a) indicate the St Anna Trough (SAT) and Laptev Sea regions, respectively, used in Table 2.

those in the Laptev Sea being most intense (Tamura and Ohshima 2011). Several models have a permanent sea ice cover over both SAT and the Laptev Sea (magenta contours on Fig. 7), a result previously explained notably by their cold air bias (Davy and Outten 2020), making it unlikely that they can open polynyas there. We nonetheless computed the polynya probability at each grid cell over the 30 winters of our study period (supp Fig. A4). Note that polynya statistics and variability in the Arctic in CMIP6 models would deserve a study of their own, and that what we present here is but a brief analysis. Most models have polynyas nearly every year in the Barents Sea (ca 10-60°E), albeit in the southern part, not by the shelf break. In the Kara Sea / SAT sector (ca 60-100°E), only CESM2, CanESM5, EC-Earth3, IPSL-CM6A-LR, MPI-ESM1-2-HR, and MRI-ESM2-0 have polynyas more than 20/30 years, often by the coast. Interestingly, the overflowing models GFDL-ESM4, MIROC6, and NorESM2-LM have polynyas by SAT only 10/30 years. For most models, the polynya frequency is further reduced in the Laptev Sea (ca 100-145°E), but it remains non-zero for 9/14 models, especially when considering the daily sea ice (supp Fig. A4, bottom panels). In summary, most models represent SAT in their bathymetry and have polynyas there; they tend to not have any trough on the Laptev Sea, but have polynyas at the shelf break. We would therefore expect them to have overflows, at both locations.

One possibility is that the polynyas do not result in cold saline (dense) water on the shelf. The two GFDL models are the only ones with extremely dense water on the shelf (Table 2), with a maximum density more than 1 kg m^{-}3 denser than the multi model average and that all other models, both by SAT and the Laptev Sea. In SAT, the other overflowing models, MIROC6 and NorESM2-LM, also are above the MMM but not strongly (37.56 and 37.81 kg m^{-}3, compared to 37.53 kg m^{-}3). The reason for their strong densities also varies between models: the GFDL models are both salty and cold, while MIROC6 is fresh and cold, and NorESM2-LM salty and warm. In fact, 6/14 models have a minimum temperature above freezing by SAT, and this number increases to 8/14 in the Laptev Sea. The spatial and seasonal variability of the properties show no consistency with overflow presence (Table 2). The apparent disconnect between shelf properties and sea ice behaviour may be the result of the sea ice models. Their detailed analysis is beyond the scope of this paper, but it is worth noting that the four families of sea ice models (CICE, COCO, LIM, and SIS) all simulate virtual salt fluxes instead of actual brine rejection (see references listed in Table 1). CICE, COCO and SIS all have a constant sea ice salinity anyway (4, 5 and 5 psu, respectively), while that of LIM is not constant but restored every 20 days. In conclusions, the presence of overflows seems unrelated to the bathymetry and presence of polynyas, and rather related to vertical grid type and shelf properties: the z-level models's dense water is most likely diluted by mixing before/shortly after it has reached the shelf break. The GFDL models, which are z* till 1000 m depth, have such extremely high densities that these high values survive the mixing. Meanwhile, NorESM2-LM and MIROC6, thanks to their isopycnic and terrain-following grids, respectively, have overflows despite a barely-above-average shelf density. These models most likely have no overflows in the Laptev Sea because they are warmer and/or fresher there.

Another process that can ventilate the deep ocean is deep convection. The Arctic Ocean is too stratified for open ocean deep convection to occur (Rudels and Quadfasel 1991). However, using the high resolution climate model HiGEM and a four times increase in CO_2 scenario, Lique and Thomas (2018) found that open ocean deep convection can start in the central Arctic. Considering that the models in this study are less stratified than observations (subsection 3a), we verify whether they ventilate the deep Arctic via open ocean deep convection by studying their maximum mixed layer depth reached over the entire 1985-2014 period. The only model with deep mixed layers in this study is GFDL-CM4, which reaches a maximum of 1815 m in the Nansen basin (Fig. 8 - note the logarithmic colour scale). The second deepest is EC-Earth3, with a maximum of 536 m. All the other models have mixed layers shallower than 100 m on average over the deep Arctic basins, never exceeding 250 m. Considering that we found a deep bias in the Atlantic layer, this means that GFDL-CM4 and EC-Earth3 are the only two models whose mixed layers can reach below the halocline. As previously discussed, GFDL-CM4's Atlantic layer extends deeper than 2000 m, so its comparatively deep mixed layer still cannot ventilate the deep and bottom waters.

In summary, we found three models that show indications of dense water overflows in St. Anna Trough that may penetrate below the Atlantic Water, and two models that may ventilate the Atlantic layer via open ocean deep convection.

Table 2. For each model and the multi-model mean (MMM), statistics, seasonal cycle and spatial differences in bottom density, bottom salinity, and bottom temperature over the St Anna Trough (SAT) and Laptev Sea regions (shown on Fig. 7), which can impact the formation of overflows. Density and Salinity: temporal maximum of the geographical maximum; difference between the temporal maximum and minimum of the geographical maximum; temporal maximum of the geographical standard deviation. Temperature: temporal minimum of the geographical minimum; difference between the temporal maximum and minimum of the geographical minimum; temporal maximum of the geographical standard deviation.

		Density (kg m^{-3})			Salinity (psu)			Temperature (°C)		
Model	Region	Max	Seas.	Spatial	Max	Seas.	Spatial	Min	Seas.	Spatial
BCC-CSM2-MR	SAT	37.23	0.01	0.91	35.04	0.02	1.28	1.79	0.08	1.30
	Laptev	37.23	0.01	2.63	35.05	0.01	3.37	1.83	0.02	1.28
CAMS-CSM1-0	SAT	37.10	0.01	2.09	34.85	0.03	2.76	1.52	0.17	1.00
	Laptev	37.12	0.01	3.87	34.86	0.01	4.98	1.55	0.03	1.17
CESM2	SAT	37.37	0.16	0.37	35.12	0.12	0.60	0.74	1.36	1.12
	Laptev	37.22	0.04	2.48	34.98	0.04	3.20	1.38	0.23	1.88
CanESM5	SAT	37.42	0.31	0.44	34.89	0.48	0.56	-1.73	2.42	1.20
	Laptev	37.22	0.06	4.23	34.62	0.05	5.12	-1.03	0.42	4.16
EC-Earth3	SAT	37.64	0.50	0.16	35.34	0.65	0.24	-2.19	4.26	0.85
	Laptev	37.80	0.65	2.33	35.39	0.95	2.64	-1.89	2.50	2.91
GFDL-CM4	SAT	38.71	1.29	0.42	36.37	1.60	0.59	-1.96	1.41	1.33
	Laptev	41.07	3.90	3.77	39.32	4.80	4.66	-2.11	3.61	3.41
GFDL-ESM4	SAT	39.32	1.91	0.73	37.13	2.37	0.97	-2.00	2.85	1.03
	Laptev	40.50	3.19	3.68	38.61	3.95	4.42	-2.08	2.69	4.08
GISS-E2-1-H	SAT	36.94	0.15	0.51	34.31	0.08	0.69	-1.00	1.49	0.58
	Laptev	37.23	0.04	1.70	34.53	0.02	2.15	-1.80	0.45	0.58
IPSL-CM6A-LR	SAT	37.50	0.36	0.13	35.07	0.53	0.23	-1.87	3.81	1.14
	Laptev	37.91	0.75	2.38	35.53	1.05	2.97	-1.82	2.64	3.90
MIROC6	SAT	37.56	0.22	0.18	34.94	0.18	0.05	-1.77	1.30	1.33
	Laptev	37.18	0.06	0.03	34.85	0.08	0.06	0.82	0.53	0.21
MPI-ESM1-2-HR	SAT	37.56	0.51	0.38	34.92	0.64	0.53	-1.90	4.08	1.11
	Laptev	37.53	0.45	4.22	34.90	0.42	5.28	-1.90	2.94	2.60
MRI-ESM2-0	SAT	37.39	0.24	0.29	35.09	0.33	0.46	-0.42	2.05	0.82
	Laptev	37.16	0.03	1.85	34.92	0.05	2.31	1.50	0.15	1.87
NorESM2-LM	SAT	37.81	0.23	0.46	35.57	0.42	0.62	-1.18	1.81	0.50
	Laptev	37.48	0.00	3.59	35.06	0.03	4.48	-0.38	0.24	2.05
UKESM1-0-LL	SAT	37.64	0.32	0.61	35.12	0.33	0.77	-1.89	2.79	0.65
	Laptev	37.36	0.06	3.50	34.82	0.07	4.38	-0.74	0.36	3.33
MMM	SAT	37.53	0.28	0.43	35.08	0.38	0.59	-1.75	1.93	1.07
	Laptev	37.30	0.06	3.07	34.95	0.06	3.87	-0.89	0.44	2.32

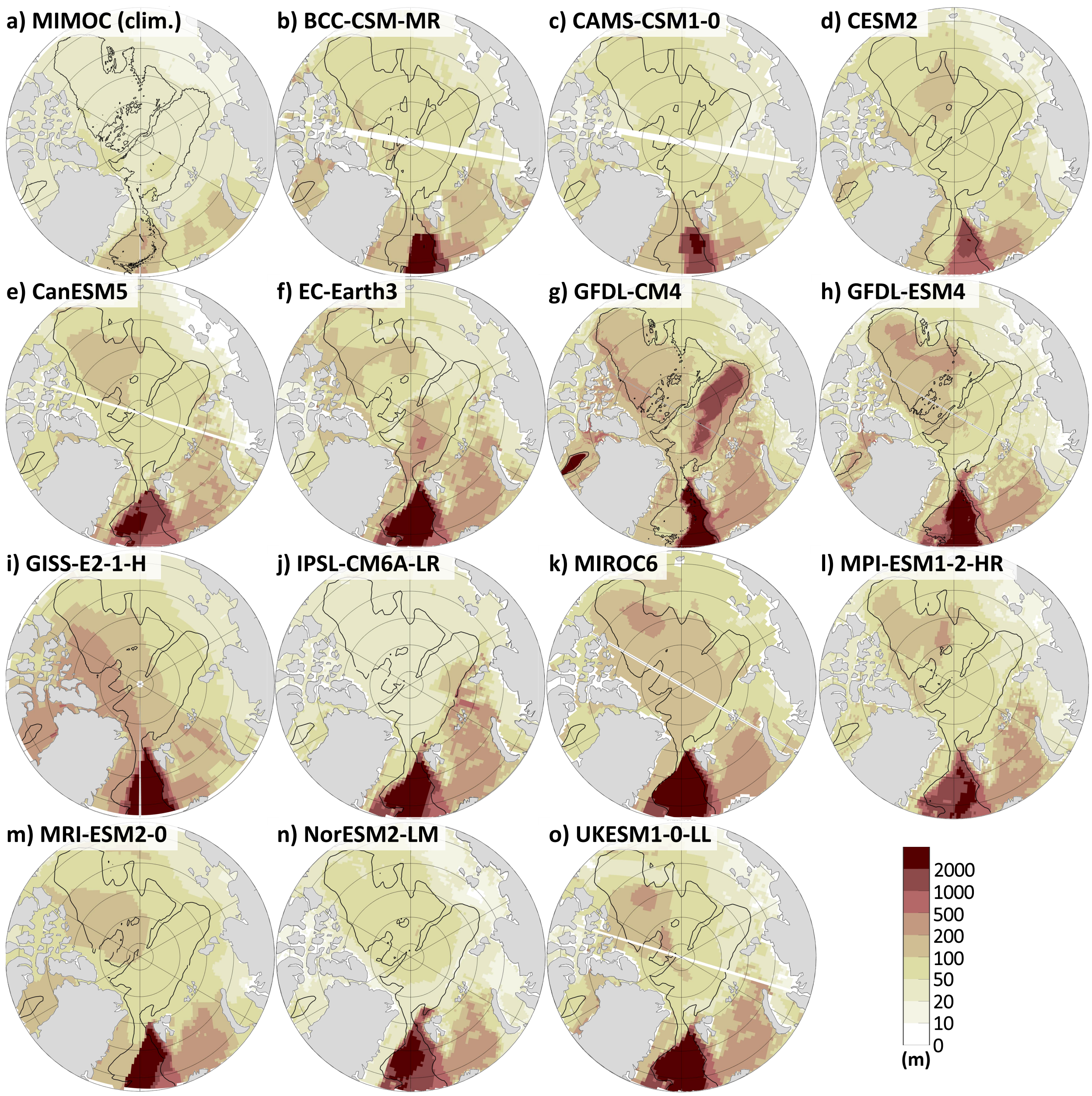

502 FIG. 8. a) Maximum of the monthly climatological mean mixed layer depth (MLD) from MIMOC (Schmidtko et al. 2013); b)-o) Maximum mixed layer depth over the period January 1985 - December 2014 for each CMIP6 model. Note the logarithmic colour scale. On each panel, the black contour is the 2000 m isobath from a) GEBCO and b)-o) the individual models.

c. Circulation of deep water masses within the Arctic

We now investigate the representation of the ocean circulation in the Arctic, first for the subset of models that provided the age of water output. Tanhua et al. (2009) estimated the age of water in the Arctic Ocean from transient tracer measurements (Fig. 9a). The age of water in the models depends strongly on whether the models followed the OMIP protocol (Griffies et al. 2016), which recommended that the model age be reset to 0 at the beginning of the historical run. In CESM2, CanESM5, IPSL-CM6A-LR, NorESM2-LM instead the age was set to 0 before the spin-up began and not reset since (personal communication with the individual modellers listed in the acknowledgments, March 2022). Note that for the study we conduct here, the latter method is most desirable. Therefore, we instead compare the models' normalized ages, as was done by Dufour et al. (2017), i.e. the age in the Arctic divided by the maximum age, globally, by the end of the historical run (given in the panel titles of Fig. 9).

In the upper ocean (top panels of Fig. 9), most models seem to "spill over", i.e. below 100 m depth, the age gradually increases from the shallow levels of the Nansen basin by the Kara Sea (to the right, true age is 0) towards the deep parts of the Canada basin by Alaska (to the left, true age is larger than 100 years). Notable exceptions are CanESM5 (c) and NorESM2-LM (h) who have waters that are much older than the observations between 200 and 1000 m depth throughout most of the deep Arctic (up to 500 years older for CanESM5), albeit with a mild doming of young waters deeper over the Mendeleev Ridge - opposite to the observations. In the deep ocean (bottom panels of Fig. 9), all models reproduce the contrast between the Eurasian basin (right) and the Canadian basin (left): in the deep Eurasian basin, waters are younger to a deeper level than in the Canada basin. All models also show a latitudinal gradient in age at any depth, with the exception of IPSL-CM6A-LR whose age primarily increases with depth. Finally, the overflows of MIROC6 and NorESM2-LM are once again visible, as a flow of water of age 0 on the shelf in the upper panels then a bulge of young water in the upper right corner of their bottom panels. In fact, the age sections even suggest that MPI-ESM1-2-HR (Fig. 9f) and MRI-ESM2-0 (g) might have occasional overflows.

Both mixing and large scale circulation could be responsible for this age distribution. The evolution of age with depth-only in IPSL-CM6A-LR in particular could be caused by its comparatively simple turbulent closure schemes (Madec 2008); yet UKESM1-0-LL and its even simpler linear diffusivity scheme have a somewhat accurate age distribution. Another option is that, as found by Muilwijk et al. (2019) who used passive tracers in a coordinated study of 9 ocean models, the Atlantic Water flow pattern in the Arctic Ocean is highly inaccurate. Here, the strong significant across-model correlation between the age of the Atlantic Water on the Greenland shelf and its temperature (-0.71, i.e. older water is colder) also suggests that the circulation may be inaccurate in CMIP6 models. In observations, the journey of the Atlantic Water across the Arctic can be retraced based on its properties once it reaches the Greenland shelf: the shorter route across the Lomonosov Ridge involves less modification than the long route around the Canada basin, so this younger water is also warmer (e.g. Rudels 2012). Therefore, in the models with the older and colder water, the flow may be slower than in the models with younger and warmer waters, or the flow may be taking different routes. We therefore now investigate the velocity fields of the models.

We compare one of the "young" models, MIROC6, and the "oldest", CanESM5, in Fig. 10. These two models were chosen because their horizontal grids are not significantly rotated compared to the Cartesian reference (see supp. Fig. A1), therefore the velocity components 'uo' and 'vo' are meaningful on the models' grids. The value of the velocity is shown for all other models on supp. Figs. A5 and A6. Note that there are no observational datasets of velocity in the deep Arctic, but the reader can find a detailed explanation of the path of each water mass in Rudels (2012). As expected, these two models differ significantly both in the magnitude of their ocean velocity and in its direction. In MIROC6 (Fig. 10a), the Atlantic Water flows in an orderly loop around the Eurasian basin at 2 cm/s or faster, i.e. the same order of magnitude as measured by the Eastern Eurasian Basin moorings of Woodgate et al. (2001) and Pnyushkov et al. (2015). The flow in CanESM5 (Fig. 10b) is four times slower and less orderly, with a lot of recirculation within the Eurasian basin. The AW also recirculates more in the Makarov basin in CanESM5 than in MIROC6, but in the Canada basin, they look somewhat similar, although again MIROC6 is twice as fast. At 2000 m, the circulation in the Eurasian basin is very similar to that of the AW for both models (Fig. 10c and d), probably because as discussed previously, the same water mass is found at the depth of the AW core as at 2000 m in most models. In MIROC6 it is no issue for the water to flow from the Makarov basin towards the Canadian shelf, but in CanESM5 the water loops around a shallow feature, most likely the model's interpretation of the Alpha Ridge. Aside from that loop, MIROC6 shows again velocities twice as high as CanESM5. The absolute velocity does

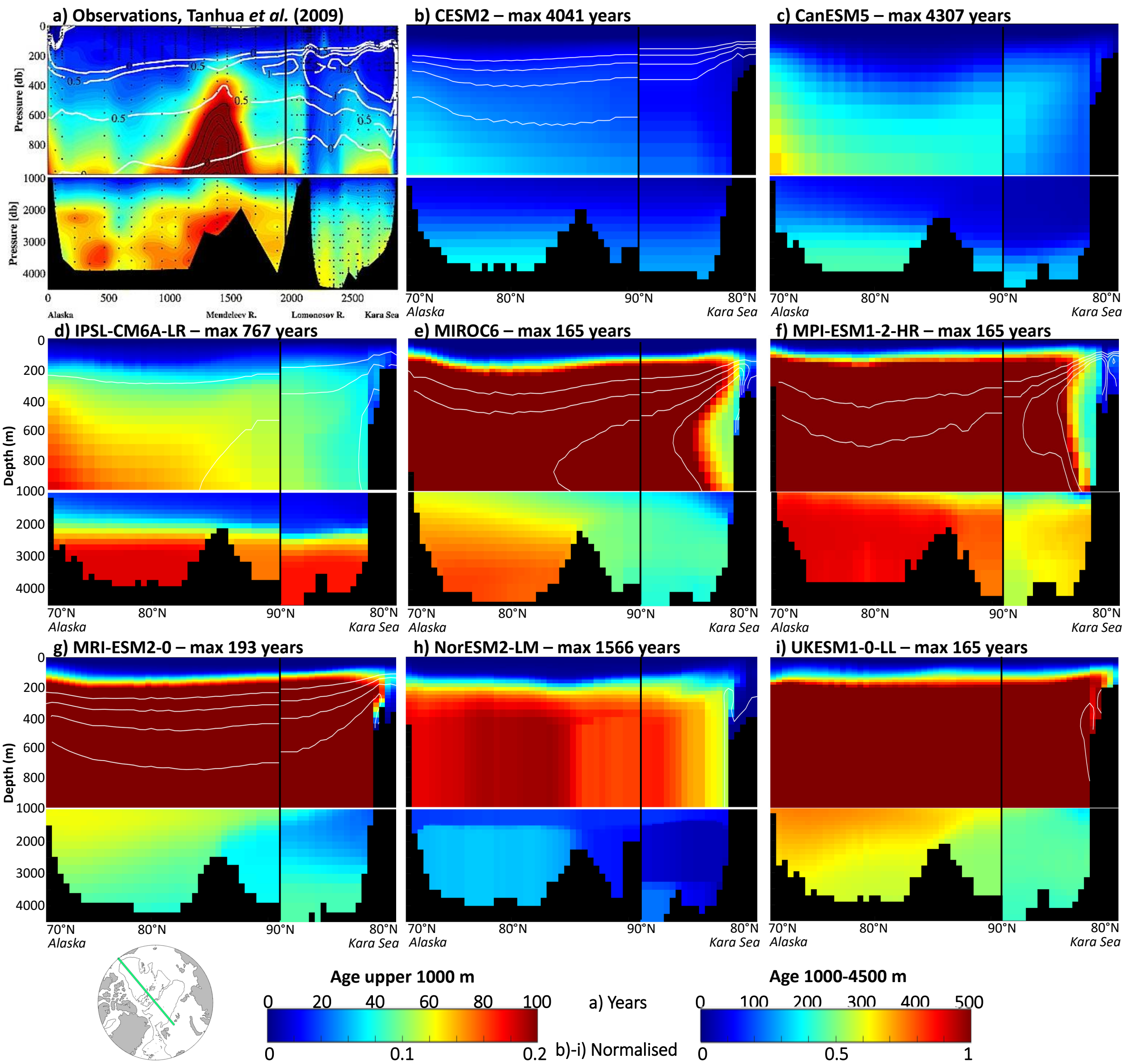

FIG. 9. Age of water across the deep Arctic basins a) as reported by Tanhua et al. (2009) (reproduced with permission from John Wiley and Sons, license number 5239230975302) and b)-i) for the 8 CMIP6 models of our study that provided this output, normalised relative to each model's maximum age in the run (given in the title of each panel). See Tanhua et al. (2009) for exact locations of their measurements; in CMIP6 models, section goes along 140°W to the North Pole, then along 40°E (green line on the map, bottom left corner). Black vertical line marks the Canadian-Eurasian basins separation. White lines on top panels, the 0, 0.5, 1, and 1.5°C isotherms.

not seem to be the key element for ventilation though; for example, CESM2 and UKESM1-0-LL (supp. Fig. A5c and l) have similar velocities in each basin, yet very different ages, even taking

UKESM1-0-LL's age reset into account. IPSL-CM6A-LR and NorESM2-LM in contrast have similar ages but very different velocities both in the Atlantic layer and at 2000 m depth (supp. Figs A5 and A6, h and k), with NorESM2-LM being up to 100 times faster than IPSL-CM6A-LR locally. In summary, the age difference on Fig. 9 likely is the result of a more coherent flow rather than flow speed only, both in the Atlantic layer and deeper.

What causes these differences in circulation? We find significant, negative across-model correlations between the depth of the Atlantic Water core and its velocity in each basin (-0.47 in the Nansen basin; -0.62 Amundsen; -0.46 Makarov; -0.42 Canada). That is, the slower the core, the deeper. It is unclear however what the causality is, i.e. whether the flow is slower because it is deeper or deeper because it is slower. Another thing we notice is the impact of horizontal resolution, notably when comparing the higher resolution GFDL-CM4 (9 km) to the others (40-50 km): at this resolution, the meanders and recirculations can be clearly represented (supp. Fig. A5e). The effect of resolution on Arctic circulation was also investigated by previous studies: for example, Docquier et al. (2019) and Docquier et al. (2020) show that higher ocean resolution intensifies the Atlantic Water currents and allows to better resolve the different oceanic pathways into the Arctic. Docquier et al. (2020) further note that eddy-permitting ocean resolution results in improved circulation in comparison to observations, as we see with GFDL-CM4. Roberts et al. (2016) also found that a higher ocean resolution leads to stronger boundary currents. Furthermore, differences in model diffusivity may result in different flow speeds – for example, despite having similar overall volume transports, models with higher diffusivity can have low biases in velocity as the currents are less confined to the coastal boundaries (as was found for the North Atlantic by Talandier et al. 2014) and vice versa for models with low diffusivity. Atmospheric biases is another likely explanation for differences in Atlantic Water flow speeds and patterns, as recently demonstrated by Hinrichs et al. (2021) whose realistic Atlantic Water circulation worsened after coupling to a biased atmospheric model. Finally, Karcher et al. (2007) showed that for early versions of Arctic Ocean models, the balance of potential vorticity is also important and closely linked to the intensity and the pattern of Atlantic Water flow. Steep topographic features such as the Lomonosov Ridge can create a potential vorticity barrier, thus differences in the momentum advection schemes and momentum closure schemes, and obviously, in the bathymetry representation (Fig. 7), might also lead to differences among the models.

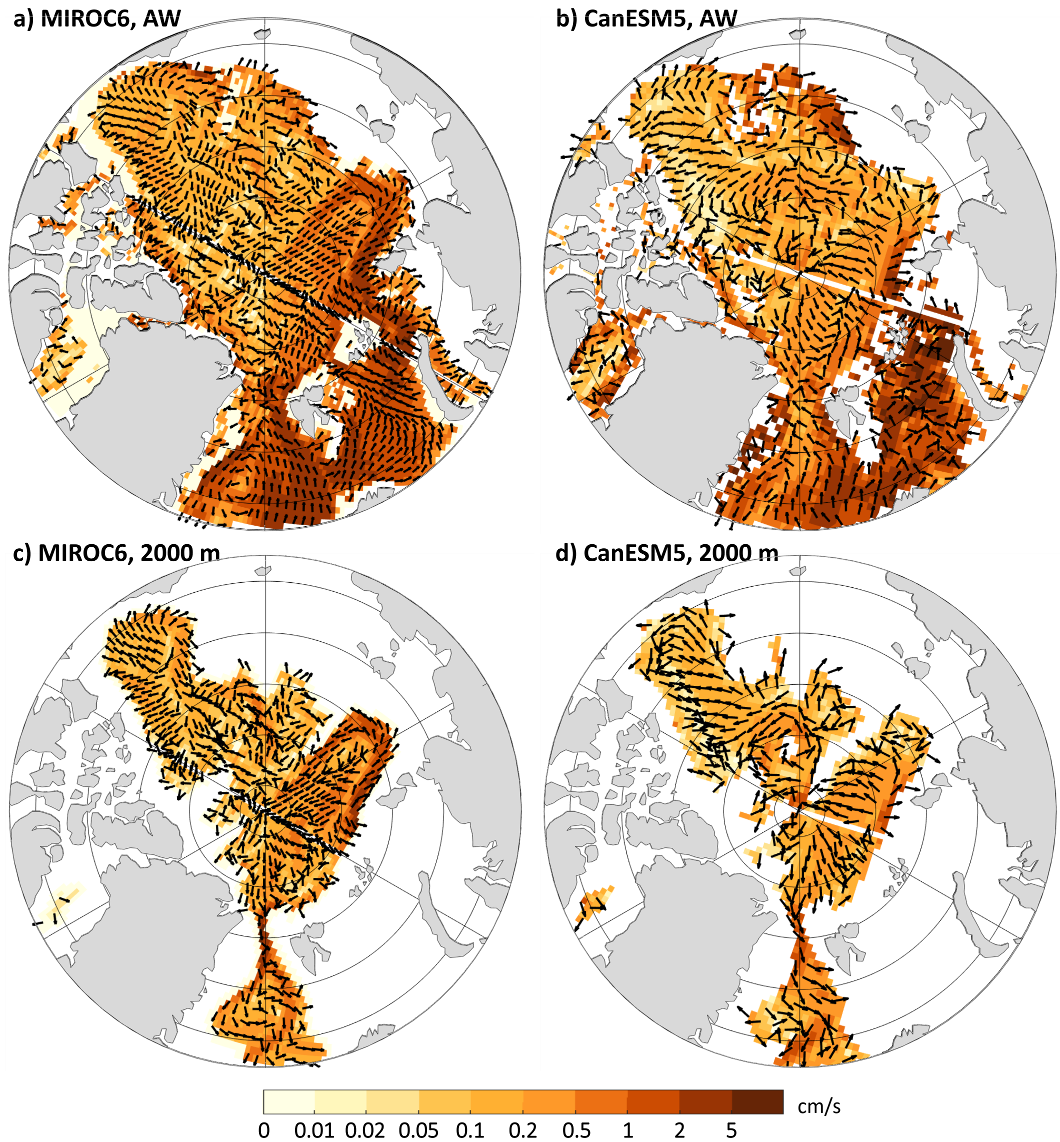

Fig. 10. Velocity (shading) and direction of the flow (arrows) for one of the models with the youngest deep waters, MIROC6 (left, horizontal resolution 39 km), and the one with the oldest, CanESM5 (right, horizontal resolution 50 km), at the Atlantic Water core depth of each grid cell (top) and 2000 m depth (bottom). Note the logarithmic scale for the velocity. For increased readability, the velocity vectors have been normalised, so all arrows are of the same length. The velocity norm is provided for all the other models in supp. Figs A5 and A6.

In summary, in this subsection we have shown that differences in model ages (even accounting for their different protocols) seem linked to a more coherent flow. Such flow efficiently transports the water from the Nansen to the Canada basins, suggesting that what enters the Arctic through Fram

Strait controls the properties in the whole deep Arctic. In the following subsection, we therefore investigate these flows through Fram Strait.

d. Exchanges through Fram Strait

The representation of Fram Strait in our selection of CMIP6 models is quite biased, be it in properties or in fluxes. When compared to WOA18 (Fig. 11), most models are biased cold in the upper ocean where WOA18 is warm, and biased warm in the deeper layer where WOA18 is cold. In other words, their temperature contrast between the upper and deeper ocean is too small. We observe the same pattern in salinity to some extent (supp. Fig. A7), with strong saline biases in the upper ocean towards Greenland (left of the panels) where WOA18 is freshest, but in the rest of the strait there is no across-model consistent bias. The biases in Fram Strait have a strong and significant across-model correlation to the property biases in the Nansen basin described previously: 0.84 between the Fram Strait inflow and the Nansen basin Atlantic Water core for the salinity and 0.74 for the temperature, reduced to 0.78 and 0.56 respectively when comparing the Fram Strait inflow to the Nansen basin bottom properties. The Nansen basin biases are also strongly correlated to the bottom property biases in the Nordic seas (Heuzé 2021), the largest correlation being 0.81 (0.83) between the Nordic Seas bottom salinity (temperature) and that in the Nansen basin at 2000 m depth, suggesting that the biases are advected from the south (upstream of Fram Strait) and into the Arctic. We verify this hypothesis below.

The location of the inflows and outflows is also inconsistent across models (black contours, Fig. 11). Using the moorings deployed across Fram Strait, Beszczynska-Möller et al. (2012) showed the presence of a strong outflow, i.e. flow out of the Arctic, to the west, a strong inflow to the east, and several recirculations in the centre of the strait (schematically represented on Fig. 11a). Although both in- and outflows are in fact each composed of several water masses (von Appen et al. 2015), the longitudinal patterns are nonetheless quite consistent through depth. The models show instead a large range of behaviours, for example:

- BCC-CSM2-MR and CAMS-CSM1-0 do not simulate a separation by longitude but by depth, where the upper ocean is an outflow, intermediate depths (the majority of the water column) is an inflow, and anything below 2000 m is again an outflow;

- CanESM5, EC-Earth3, IPSL-CM6-A-LR, MPI-ESM1-2-HR and UKESM1-0-LL simulate an inflow that is limited to a strong core along the east coast, extending no deeper than 1000 m;
- GFDL-CM4, GISS-E2-1-H and MRI-ESM2-0 simulate an outflow to the west and inflow to the east, which is correct. They however lack the observed recirculations (i.e. alternation of in- and outflows) to be deemed accurate.

Fram Strait is biased warm and the location and extent of the in- and outflows are inaccurate in all models, at least when compared to the mooring data of Beszczynska-Möller et al. (2012). It is therefore not surprising that the heat and volume fluxes through Fram Strait are inaccurate as well. Note that as the salt fluxes strongly resemble the volume fluxes and uncertain observational values were only mentioned in Marnela et al. (2016), we limit our discussion to the heat and volume fluxes. Besides, in contrast to observational data, the models do not have distinct east/west and upper/deeper fluxes. We therefore discuss here the full-depth net fluxes into and out of the Arctic, i.e. the sum of the positive and negative fluxes, respectively. For the heat flux (Fig. 12a), most models are within the observational range, except for GFDL-CM4, MIROC6 and MRI-ESM2-0 who overestimate both the inflow and outflow. For example with a 30-year mean value of 61.6 ± 7.1 TW, the inflow in MIROC6 is nearly twice as large as that computed by Schauer et al. (2004) over 1997/1998 (31.8 TW). All models correctly simulate that the transport of heat into the Arctic is larger than the transport out (difference of height between the bars), but this difference ranges from 1.4 TW for EC-Earth3 to 37.0 TW for MIROC6. One caveat is that where observational values are computed relative to different reference temperatures, we here computed them all relative to 0°C in order to better compare the models to each other. We argue that as all the models of this study are biased warm in Fram Strait (Fig. 11), and that the across-model correlation between heat flux and temperature bias is only 0.49, i.e. explains only 24% of the variance, choosing a common reference temperature is not the leading reason for the differences between models and observations.

Unlike the heat flux, the volume flux is underestimated in the majority of our models (Fig. 12b). The volume flux is the integral of the velocity through Fram Strait (see eq. 1), while the heat flux is the integral of that velocity multiplied by the temperature through the same section (see eq. 3). So first, the volume flux underestimation means that the strong warm bias in Fram Strait dominates the heat flux values. Regarding the volume, only the inflow of GFDL-CM4 and GISS-E2-1-H are within the observational range (averaged from Beszczynska-Möller et al. 2012; Marnela et al.

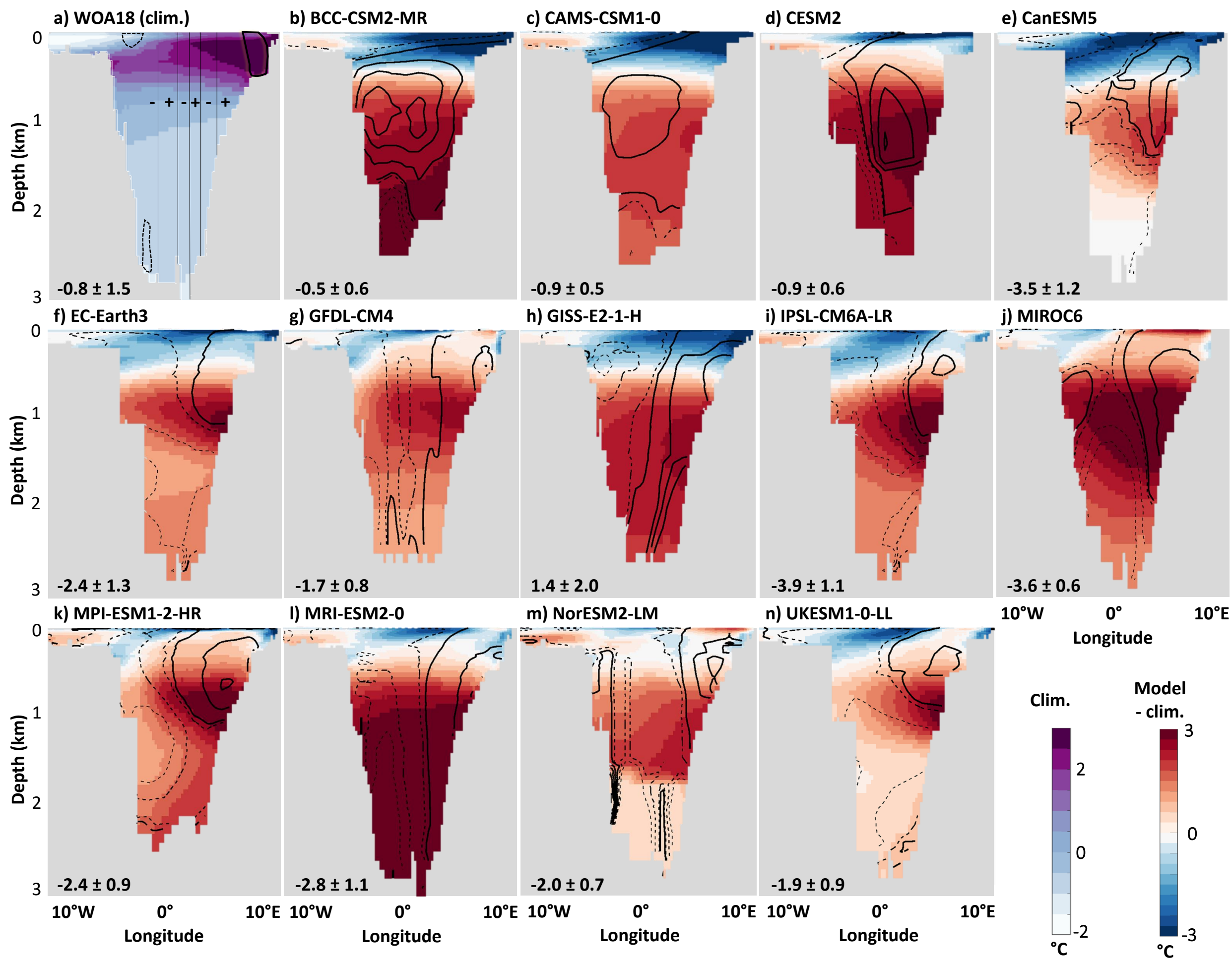

FIG. 11. a) Potential temperature across Fram Strait in WOA18; b)-n) difference between each model's potential temperature and that of WOA18 across Fram Strait (shading), along with their volume flux as black lines (0.02 Sv contours, where 1 Sv = 10^6 m^3 s^{-1}; plain means positive, into the Arctic; dashed negative, out of the Arctic). Volume flux contours are not available for observations; we instead show the positive/negative velocity regions and location of strongest velocities from Beszczynska-Möller et al. (2012) on panel a). Bottom left of each panel: net volume flux in Sv, where negative means net southward. For observations, value from Marnela et al. (2016). Salinity biases are shown in supp. Fig. A7

2016; De Steur et al. 2014; Schauer et al. 2004), and no model reaches the outflow observational range (11 ± 2 Sv, same references). Although all models except GISS-E2-1-H correctly have larger outflow than inflow, this difference is nearly twice the observational average (ca. 2 Sv) in CanESM5, IPSL-CM6A-LR and MIROC6 (3.5, 4, and 3.5 Sv on average, respectively), and less than half in BCC-CSM2-MR, CAMS-CSM1-0 and CESM2 (<1 Sv). Zanowski et al. (2021)

computed the upper ocean liquid and solid freshwater fluxes, where solid means freshwater content of the sea ice, in and out of all the Arctic gateways for 7 CMIP6 models. We use their results to determine whether the inaccurate differences between deep inflow and deep outflow through Fram Strait that we found are compensated by the flows through the other straits and/or the solid fluxes. With only 5 models in common, statistics are meaningless, but this small comparison suggests that the more total solid freshwater flux out of the Arctic, the smaller our heat and volume outflows; and the more total liquid freshwater flux out of the Arctic, the stronger our volume inflow. That is, the more sea ice out, the less heat and volume out, but the more water out, the more deep water flows in. Although these results would be logical, they should be investigated in a larger group of models; doing this here is however beyond the scope of this paper.

Could the biases in fluxes through Fram Strait explain the biases that we found in the deep water masses of the Arctic? At first glance, no: there is no across-model relationship between any of the biases described in subsection 3a and the net in- or outflows. We instead investigate the models individually and compare their fluxes to the Atlantic Water core temperature, in the Nansen basin only, as we previously showed that all property biases in all water masses and all deep basins were strongly correlated with each other. We find for all models strong positive correlations between the fluxes and time series of the properties (see two exemplary models on Fig. 13), but no across model consistency. That is, some models have their strongest correlation with the heat flux, while others with the volume flux (not shown). But more importantly, for all models the whole inflow is not consistently correlated to the properties: for some, a specific longitude has most of the positive correlation (Fig. 13a); others have distinct patches, similar to what is expected from observations (Fig. 13b, note the upper and lower patches, separated at approximately 1500 m depth).

In summary, for all models, we do find strong positive correlations between at least part of the inflow and the biases in properties in the deep Arctic. The volume fluxes are biased low in most models, which coupled with the fact that Fram Strait is biased warm, results in seemingly accurate heat fluxes through Fram Strait. Nevertheless, it would be desirable to understand why the volume fluxes are inaccurate. In observations, heat and volume fluxes have their largest values in winter, typically February/March, and lowest values in spring/summer, typically June (Schauer et al. 2004; Beszczynska-Möller et al. 2012; De Steur et al. 2014). In our models, the majority follow this pattern of maximum in winter and minimum in summer, although the maximum can

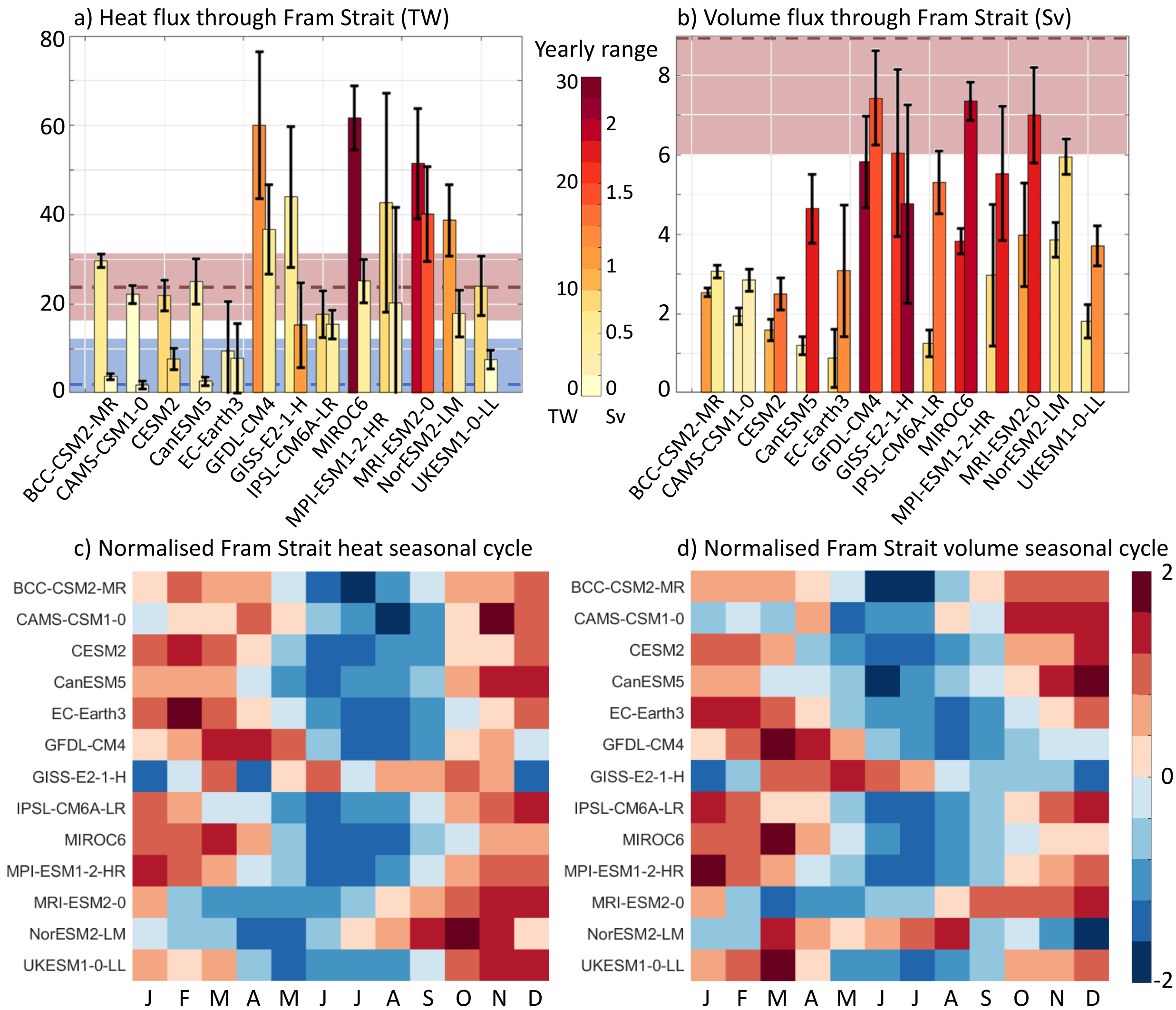

FIG. 12. For each model that provided the velocity outputs, a) Bars: absolute value of the 30-year mean heat flux, in TW, into the Arctic (left) and out of the Arctic (right); black error bars: interannual variability, i.e. spread in the yearly means; shading: difference between the yearly maximum and minimum; pink and blue boxes: range of the observational values (see text), with mean as dashed line, for the in- and out-flow, respectively. b) Same as a) but for the volume flux, in Sv (1 Sv = 10^6 m^3 s^{-1}); the observational outflow values are off-screen at 11 ± 2 Sv. c) and d), normalised seasonal cycle in heat and volume inflow, respectively.

be found in any month. The exceptions are GISS-E2-1-H and NorESM2-LM, who have their lowest values in winter for both heat (Fig. 12c) and volume (Fig. 12d). The yearly range can be large in some models (up to 32.4 TW for the heat inflow in MIROC6, and 2.3 Sv for the volume

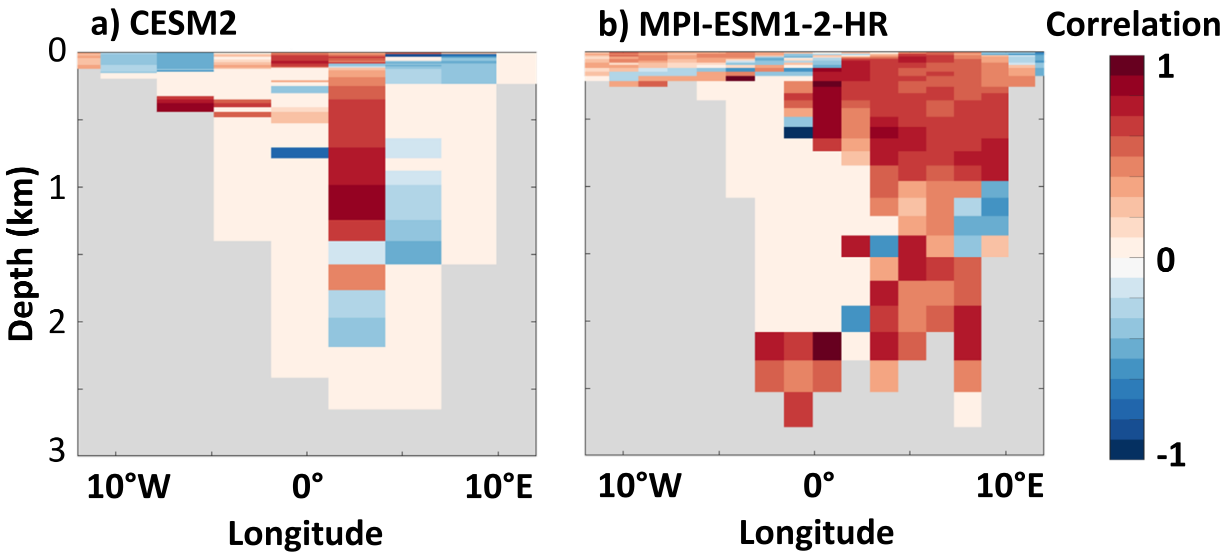

FIG. 13. For two exemplary models, maximum correlation between the time series of yearly means in Atlantic Water core temperature in the Nansen basin and the heat flux into Fram Strait of each grid cell, allowing for a lag of up to 5 years. Only significant (at 95%) correlations shown. Note that this calculation was performed on the model's native grid, hence the difference in bathymetry from Fig. 11.

inflow in GFDL-CM4), but so can it in observations (10-50 TW and 4-6 Sv Schauer et al. 2004; Beszczynska-Möller et al. 2012; De Steur et al. 2014).

The reason why the fluxes through Fram Strait are highest in winter can be found in the processes that cause them. In models (Årthun and Eldevik 2016; Muilwijk et al. 2019) as in observations (Wang et al. 2020), the heat and volume fluxes through Fram Strait are driven at least in part by the gyre and/or winter convective activity in the Nordic Seas (Smedsrud et al. 2022), regardless of the depth level considered (von Appen et al. 2015; Chatterjee et al. 2018). The convective activity values in CMIP6 models were recently published by Heuzé (2021): they showed that all the models that we consider here largely overestimate it. In particular, all models but CAMS-CSM1-0 had mixed layers deeper than 1000 m every year over 1985-2014 over an extensive region, which is visible on Fig. 8; CAMS-CSM1-0 did so only 24 out of 30 years. Comparing our fluxes with their mean deep mixed volume, i.e. sum of the cell area multiplied by the mixed layer depth (MLD) for all cells where that MLD is deeper than 1000 m, we find significant across-model correlations (at 90%) with the heat inflow through Fram Strait (0.48) and the volume outflow (0.42). That is, as in observations, a stronger convective activity in the Nordic Seas is associated with a stronger heat inflow into the Arctic, but also with a stronger volume outflow from the Arctic. These results do not prove causality but suggest a possible chain of biases:

1. The Nordic Seas have biased temperature and salinity and a biased representation of convective activity (Heuzé 2021);
2. The stronger the convective activity, the stronger the volume transport northward, through Fram Strait and into the Arctic;
3. That volume transport advects the biases in properties from the Nordic Seas to Fram Strait, so that the stronger the volume transport, the more Fram Strait is biased warm. Another possibility is that the convective activity directly sets the properties of the advected water, as has been found in observations before (Langehaug and Falck 2012);
4. The stronger the warm bias at Fram Strait, the stronger the heat flux into the Arctic.

This would explain why the "worst" models for the heat fluxes are the "least bad" for the volume fluxes: the higher volume fluxes in (and out) of the Arctic are more efficient at advecting the warm bias from the Nordic Seas into the Arctic.

4. Discussion and conclusions

In this study, we first quantified biases in the Atlantic Water in all deep basins of the Arctic. In agreement with Khosravi et al. (2022), we find that its core is too cold by 0.4°C on average, too deep by 400 m, and in half of the models the Atlantic layer extends all the way to the seafloor, i.e. the properties do not evolve with depth as they do in the real ocean. Besides, in most models the properties do not change from basin to basin. We attribute these inaccurate properties and behaviour to a lack of shelf overflows in most models, a result previously found in ocean-only simulations (Ilıcak et al. 2016), and an inaccurate flow through Fram Strait. To the best of our knowledge, no study was performed on CMIP5 models to quantify biases in deep and bottom water properties in the Arctic; we here determine that CMIP6 models are too warm by more than 1°C as multi-model average. Our findings reveal a strong decoupling between the upper layer and the rest of the deep Arctic (below 200 m), which is quite homogeneous in depth and between the basins. These biases matter for the rest of the Arctic system: We find a significant correlation between pan-Arctic sea ice volumes and Atlantic Water temperature (-0.43 at 90%), while Muilwijk et al. (subm.) find not only strong biases in the representation of stratification, but also that we cannot accurately predict future stratification changes as individual models return diverging results depending on their AW biases.

We linked these biases to processes both within and outside the Arctic. Within the Arctic, the main issue is the absence of ventilation: only three models appear to have dense water overflows, and these are taking place at only two locations (compare e.g. to the list in Luneva et al. 2020), and do not seem to ventilate the deepest layers. Our results are limited by the fact that too few models provide the age of water output, that they followed different protocols to compute it, and that a monthly resolution may be too coarse to effectively track overflows as they cascade off the shelf. Nevertheless, this finding comes as no surprise considering that the models suffer from the same overflow-issue in the rest of the world (Adcroft et al. 2019; Heuzé 2021), but this issue is particularly acute in the Arctic where no other process can replace overflows (Peralta-Ferriz and Woodgate 2015), and where open ocean deep mixing is rather indicative of inaccurate stratification (Lique and Thomas 2018). The higher resolution of CMIP6 models compared to CMIP5 was not enough to improve the overflows; in fact, it seems unlikely that such processes can ever become explicitly represented in global climate models (Fox-Kemper et al. 2019). Instead, one can notice that the three models that seem to have overflows also have isopycnal, terrain-following, or hybrid grids (Table 1). Another solution could be the widespread implementation of overflow parameterisations (e.g. Danabasoglu et al. 2010).

The biases are also related to the circulation: within the Arctic, the age of the oldest waters in the CMIP6 models studied here ranges from 122 to 1946 years (Fig. 9). Despite the models following different protocols for the age calculation, we could attribute the age difference not primarily to different flow velocities, but rather to more coherent flows. The highest resolution model had the most coherent and detailed flow, probably thanks to its eddy-permitting resolution and accurate representation of bathymetry, as discussed above. While we could speculate on the reasons for these different flow speeds and paths, we argue that such study is (still) impeded by model inconsistencies and lack of crucial metadata. Notably, we would like to see

- The ocean velocities be archived for all models;

- The necessary information to re-project the velocities onto the Cartesian grid be included in the output files, e.g. via an angle parameter that for each grid cell gives its rotation compared to the true north;

- The age of water be archived for all models;

- The age of water have the same definition for all models. In particular, resetting the age of water to 0 at the beginning of the historical run seriously impacts any study of the deep ocean;

- The spin-up time be routinely provided e.g. in the model description.

It is unlikely that continuously increasing horizontal resolutions will ultimately result in an accurate circulation, given that some flow exchanges take place in canyons, and more importantly, that high resolutions require proper eddy resolving. Promising possible solutions are model nesting (Torge Martin, personal communication, May 2022) or adaptive mesh (Wang et al. 2018), which can increase the resolution at crucial locations such as canyons or the shelf break without making computations unnecessarily heavy. At Fram Strait, we found that all models underestimate the volume fluxes in and out of the Arctic, i.e. all models are biased slow. The heat flux however appears accurate or even biased high, as the low volume fluxes are compensated by warm temperature biases at Fram Strait. We found across-model relationships between Fram Strait biases and fluxes, and inaccurate properties and deep convective activity in the Nordic Seas: as in observations (e.g. Langehaug and Falck 2012), deep convection is enhanced by the deep outflow from the Arctic and enhances the deep inflow, but also modifies the properties of the water advected through Fram Strait. The inaccurate Nordic Seas convective activity was previously blamed on inaccurate representations of sea ice extent and seasonal cycle (Heuzé 2021) and atmospheric modes of variability and wind patterns (Heuzé 2017), suggesting that detecting the cause for biases in the individual components, for example via SIMIP (Notz et al. 2016) or AMIP (Eyring et al. 2016), may be a necessary first step towards accurately modelling the coupled Arctic system. Correcting biases in the deep Arctic Ocean could even have widespread impact on the entire modelled global climate: We found significant across-model relationship between biases in the properties of the Atlantic Water in the Canada basin and that of the subpolar gyre reported by Heuzé (2021) (0.45 at 90% between the temperatures; 0.66 at 99% between the salinities), and even between the volume fluxes out of the Arctic and the Atlantic Meridional Overturning Circulation (AMOC values from Heuzé 2021, correlation of -0.43 at 90%).

Higher resolution, parameterisations and dedicated MIPs can however only go so far when there are virtually no observations to constrain the models. In the database UDASH (Behrendt et al. 2018), there are fewer than 700 full-depth hydrographic profiles in the entire Arctic north of 82°N, and only 40 of them are in winter. Consequently in their recent review, Solomon et al. (2021) did not even try to investigate the deep Arctic Ocean as there were too few observations; even for the upper ocean, they could not close the freshwater budget as Arctic river discharge timeseries were few and poor. There is an urgent need for more multi-disciplinary and multi-scale (both in time and space) observation campaigns, similar to the recently completed MOSAiC expedition (Rabe et al. 2022), across the entire Arctic, or at least for more coordination and cooperation between different expeditions to properly investigate processes and their interaction, instead of the traditional local component-specific studies.

Acknowledgments. This work was funded via Vetenskapsrådet grant 2018-03859 awarded to Céline Heuzé. Morven Muilwijk received funding from the European Union's Horizon 2020 research and innovation programme under grant agreement No 101003826 via project CRiceS. We acknowledge the World Climate Research Programme, which, through its Working Group on Coupled Modelling, coordinated and promoted CMIP6. We thank the climate modeling groups for producing and making available their model output, the Earth System Grid Federation (ESGF) for archiving the data and providing access, and the multiple funding agencies who support CMIP6 and ESGF. We are grateful to Jianglong Li (BCC-CSM2-MR), Xinyao Rong (CAMS-CSM1-0), Gary Strand (CESM2), Andrew Shao and Neil Swart (CanESM5), Thomas Reerink (EC-Earth3), the GFDL Climate Model Info Team (GFDL-CM4 and -ESM4), Gavin Schmidt (GISS-E2-1-H), Olivier Boucher (IPSL-CM6A-LR), Hiroaki Tatebe and Yoshiki Komuro (MIROC6), Johann Jungclaus (MPI-ESM1-2-HR), Shogo Urakawa (MRI-ESM2-0), Øyvind Seland and Mats Bentsen (NorESM2-LM), and Andrew Yool and Colin Jones (UK-ESM1-0-LL), for their prompt replies to our questions regarding their respective models, indicated in parentheses. We are extremely grateful to Chuncheng Guo for sending us the NorESM2-LM output when we urgently needed them but their server was down. Finally, we thank the three reviewers Hailong Liu, Carolina Dufour, and Jonathan Rheinlænder, as well as the editor Yi Deng, for their many comments that greatly improved this manuscript.

Data availability statement. All CMIP6 data are freely available via the Earth Grid System Federation. For this paper, we used the German Climate Computing Centre (DKRZ) node: `https://esgf-data.dkrz.de/search/cmip6-dkrz/` and the Geophysical Fluid Dynamics Laboratory (GFDL) node: `https://esgdata.gfdl.noaa.gov/search/cmip6-gfdl/`.

The Unified Database for Arctic and Subarctic Hydrography is freely available via `https://doi.pangaea.de/10.1594/PANGAEA.872931`. All versions of the World Ocean Atlas climatology are freely available via `https://www.ncei.noaa.gov/products/world-ocean-atlas`. All versions of the Polar science center Hydrographic Climatology are freely available via `http://psc.apl.washington.edu/nonwp_projects/PHC/Climatology.html`. The EN4 climatology is freely available via `https://www.metoffice.gov.uk/hadobs/en4/`. The gridded bathymetry GEBCO is freely available via `https://www.gebco.net/data_and_products/`

gridded_bathymetry_data/. The sea ice concentration product HadISST1 is freely available at https://www.metoffice.gov.uk/hadobs/hadisst/data/download.html.

The volume, heat, and salt flux time series have been submitted to PANGAEA in July 2022; we will add their DOI here latest during copy-editing. The routines to compute them from the CMIP6 output are freely available on Zenodo (doi:10.5281/zenodo.4606856).

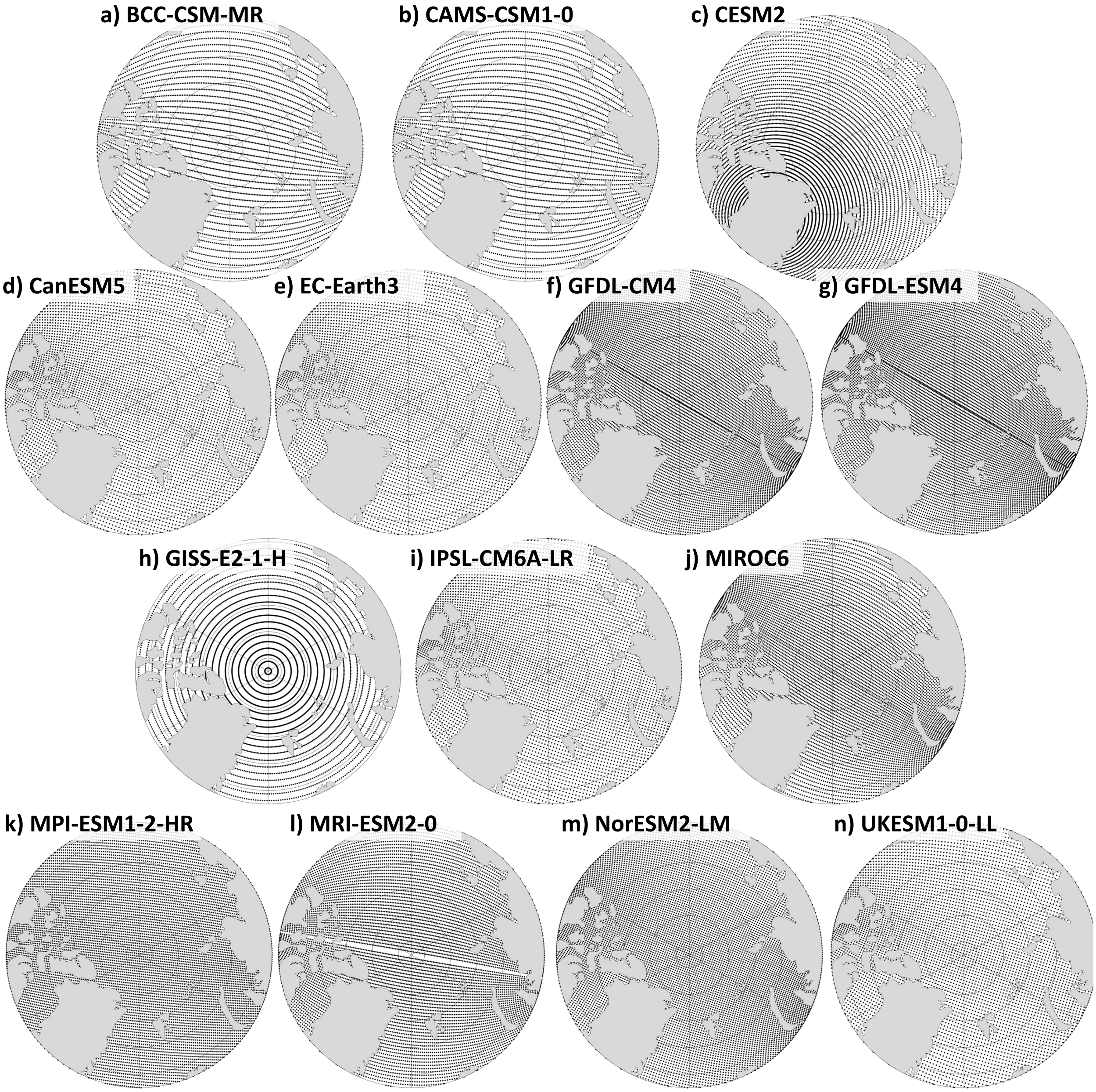

Fig. A1. Native grid of the CMIP6 models used in this study, described in Table 1. For readability, the number of grid points has been reduced by 16 and 4 for GFDL-CM4 and GFDL-ESM4, respectively.

APPENDIX

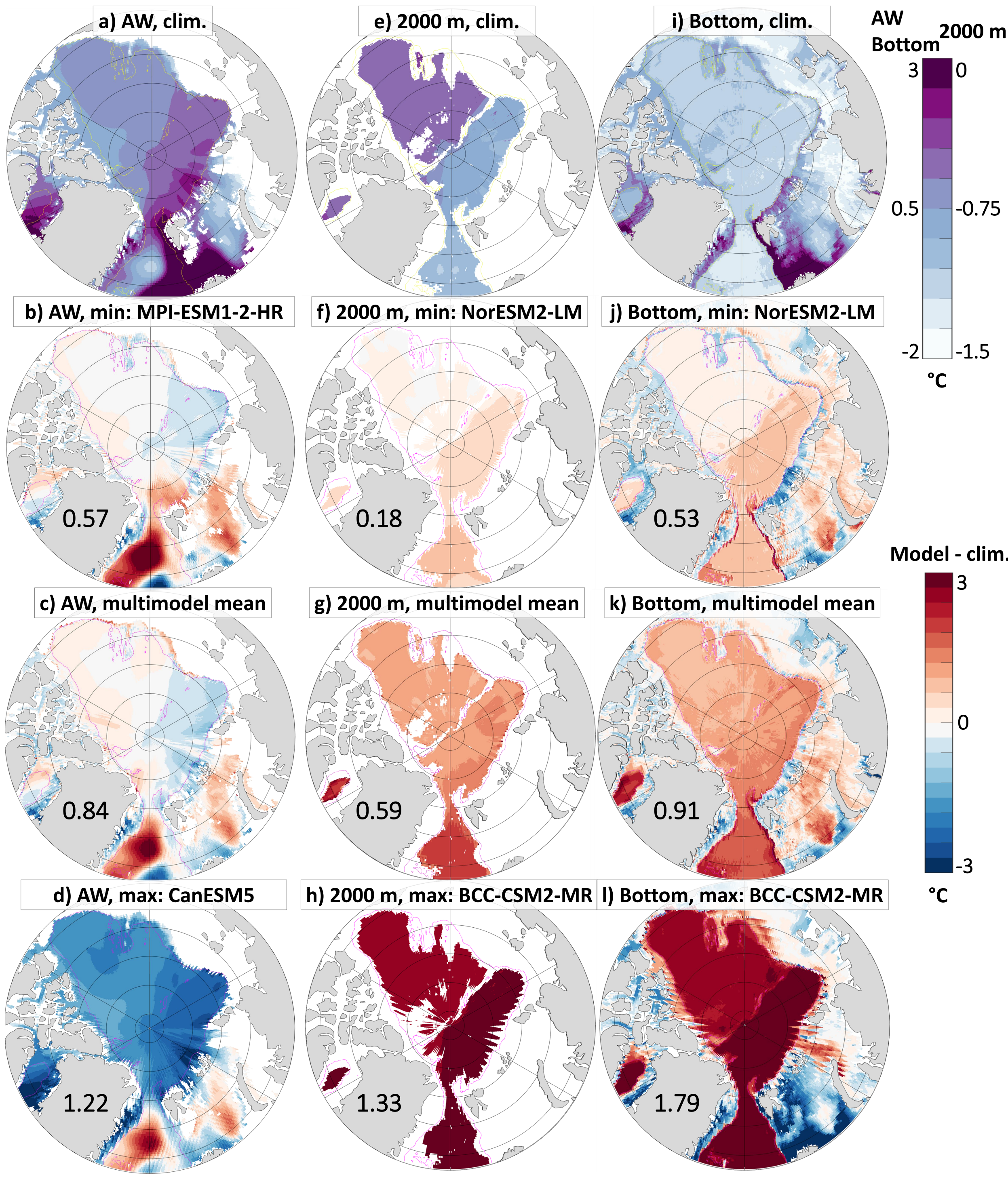

FIG. A2. Potential temperature in the WOA18 climatology (top row) and bias when compared to this climatology for the least biased model (second row), the multimodel mean (third row) and the most biased model (last row), for the Atlantic Water core (first column), 2000 m depth (second column), and the bottom (last column). Yellow line on the top row, magenta otherwise, is the 2000 m isobath. The numbers are the respective Pan-Arctic area-weighted root mean square errors. See Fig. 4 and supp. Fig. A3 for the density and salinity.

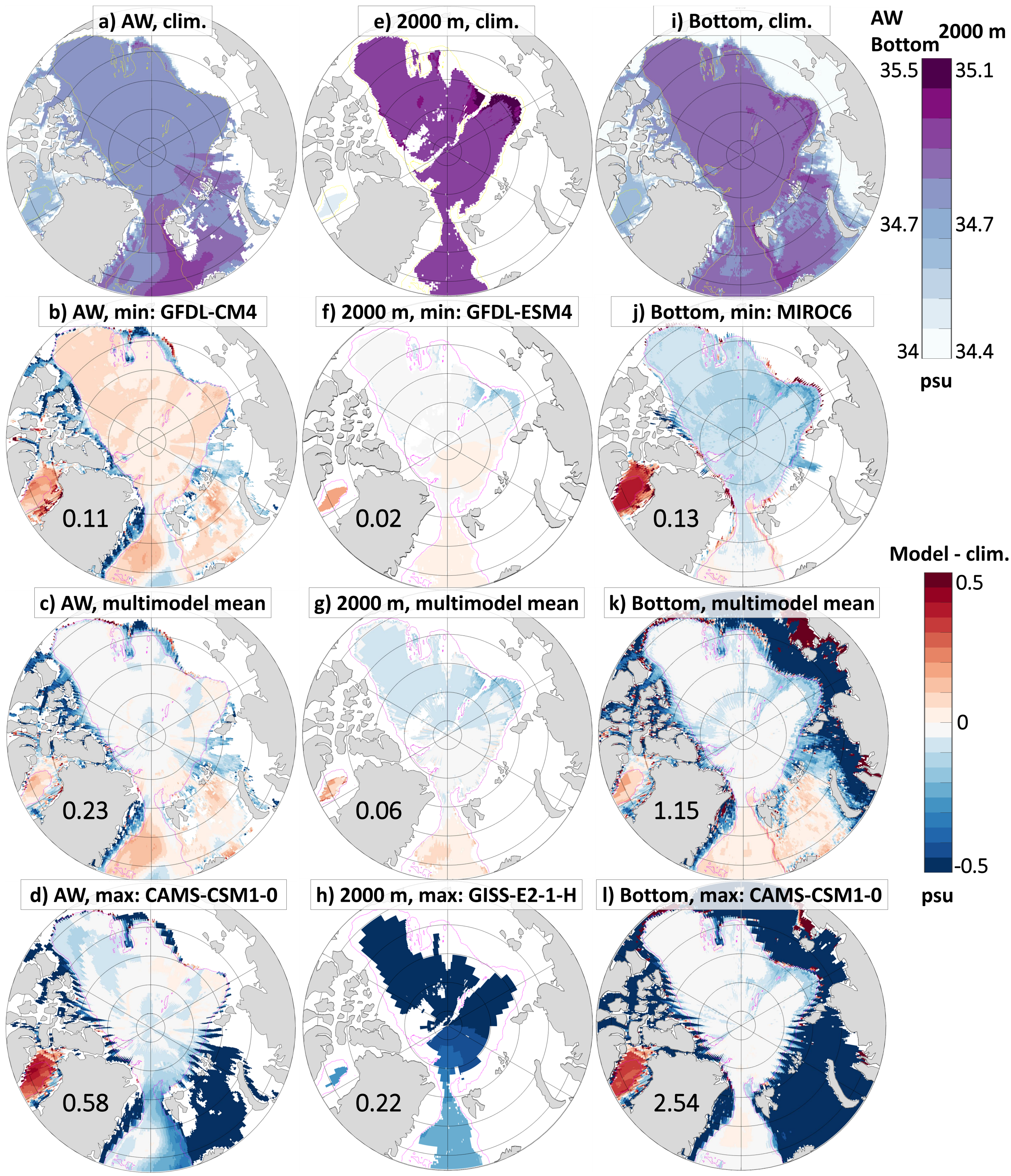

FIG. A3. Salinity in the WOA18 climatology (top row) and bias when compared to this climatology for the least biased model (second row), the multimodel mean (third row) and the most biased model (last row), for the Atlantic Water core (first column), 2000 m depth (second column), and the bottom (last column). Yellow line on the top row, magenta otherwise, is the 2000 m isobath. The numbers are the respective Pan-Arctic area-weighted root mean square errors. See Fig. 4 and supp. Fig. A2 for the density and temperature.

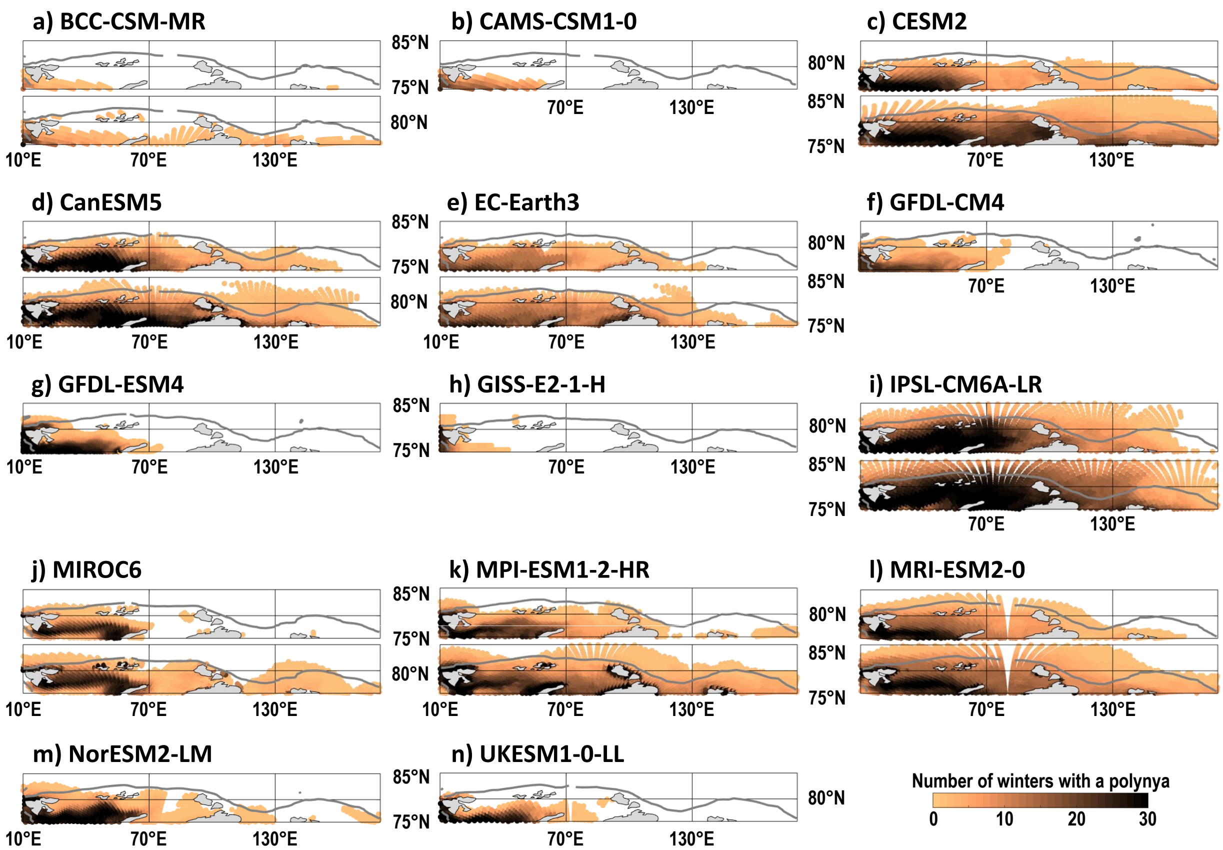

FIG. A4. For each model, for each grid cell, number of years where that grid cell features a polynya at least once during the freezing season November-March. Models are shown on their native grid. Gray line is the 1000 m isobath. Polynyas are detected using the same method as Mohrmann et al. (2021): we first flood-fill the open ocean, and then detect polynyas as having sea ice concentration lower than 60%. Top panel uses the monthly sea ice concentration; bottom panel, the daily sea ice concentration, when available.

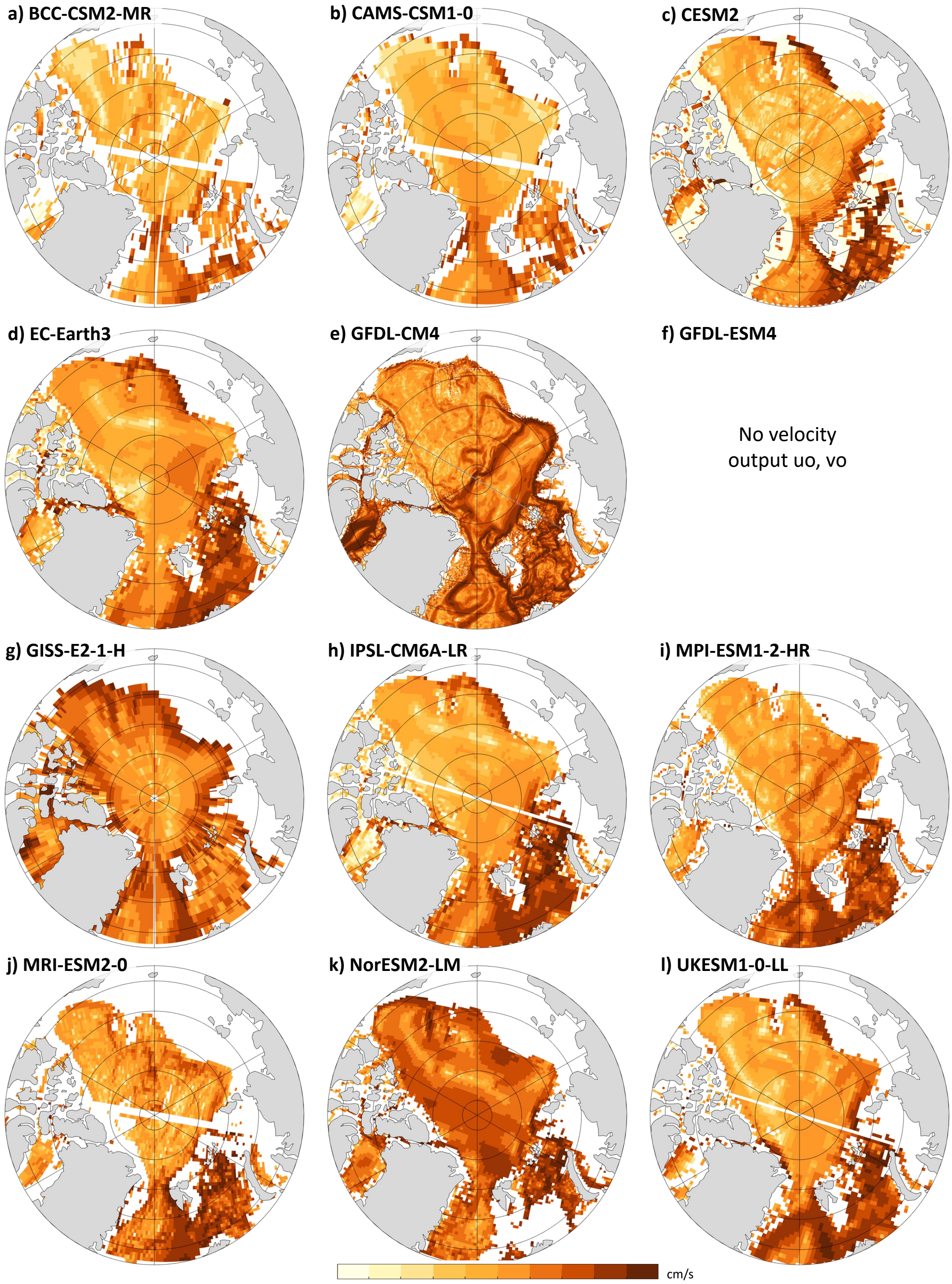

FIG. A5. Velocity of the Atlantic Water core for the models not shown on Fig. 10. Note the logarithmic scale.

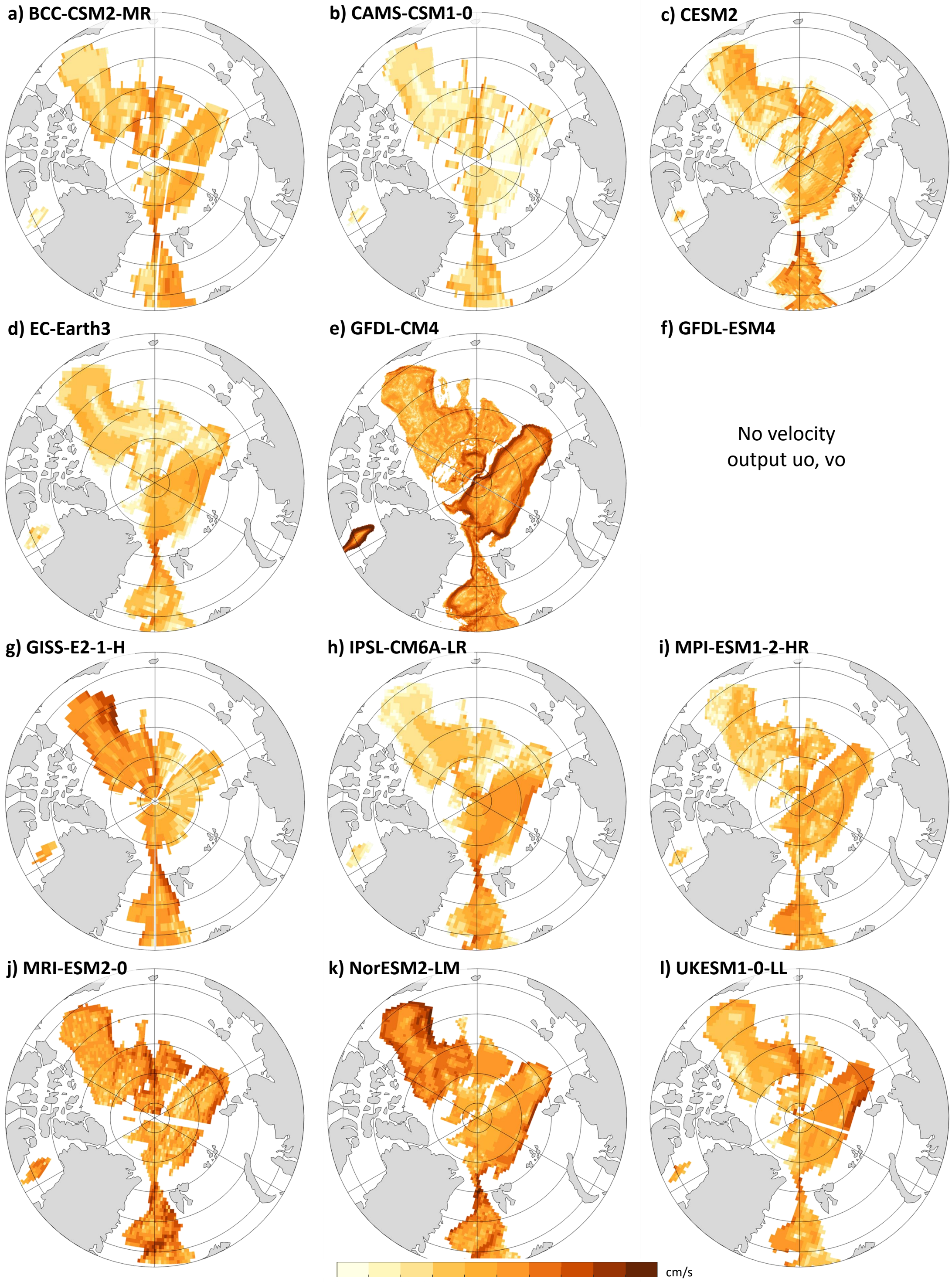

Fig. A6. Velocity at 2000 m depth for the models not shown on Fig. 10. Note the logarithmic scale.

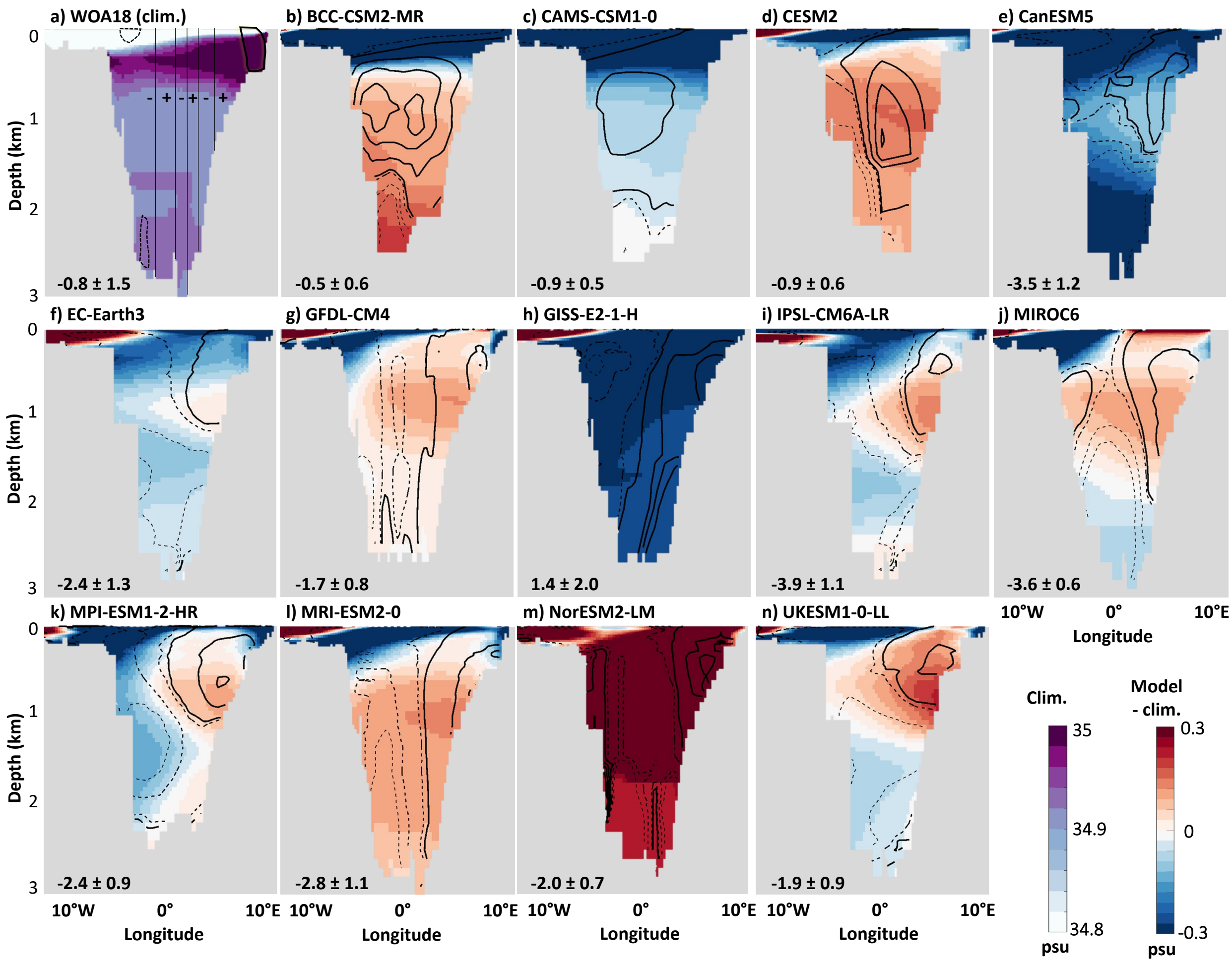

FIG. A7. a) Salinity across Fram Strait in WOA18; b)-n) difference between each model's salinity and that of WOA18 across Fram Strait (shading), along with their volume flux as black lines (0.02 Sv contours; plain means positive, into the Arctic; dashed negative, out of the Arctic). Volume flux contours are not available for observations; we instead show the positive/negative velocity regions and location of strongest velocities from Beszczynska-Möller et al. (2012) on panel a). Bottom left of each panel: net volume flux in Sv, where negative means net southward. For observations, value from Marnela et al. (2016). Temperature biases are on Fig. 11

TABLE A1. Area-weighted mean bias model minus WOA18 climatology in potential temperature (first line, left), salinity (first line, right; unit: psu), depth (second line, left) and density σ_2 (second line, right; unit: kg m^{-3}) of the Atlantic Water core for each model and the multi-model mean "MMM" in the four deep basins and on the two shelf regions of interest.

Model	Nansen	Amundsen	Makarov	Canada	Sib. Shelf	Gre. Shelf
BCC-CSM2-MR	0.27 °C; 0.23	0.72 °C; 0.27	1.12 °C; 0.31	1.27 °C; 0.35	-0.41 °C; -0.29	-0.66 °C; -0.52
	1323 m; σ= 0.14	1374 m; σ= 0.12	1332 m; σ= 0.10	1255 m; σ= 0.11	48 m; σ= -0.17	43 m; σ= -0.34
CAMS-CSM1-0	-0.02 °C; -0.07	0.38 °C; -0.04	0.75 °C; -0.02	0.81 °C; -0.05	-0.22 °C; -0.36	0.41 °C; -0.40
	368 m; σ= -0.05	376 m; σ= -0.08	363 m; σ= -0.11	206 m; σ= -0.14	35 m; σ= -0.25	36 m; σ= -0.39
CESM2	0.11 °C; 0.11	0.39 °C; 0.12	0.77 °C; 0.14	0.93 °C; 0.16	0.27 °C; 0.02	0.95 °C; 0.13
	516 m; σ= 0.08	726 m; σ= 0.04	792 m; σ= 0.01	571 m; σ= 0.01	32 m; σ= -0.01	88 m; σ= -0.03
CanESM5	-2.31 °C; -0.26	-2.12 °C; -0.25	-1.78 °C; -0.26	-1.68 °C; -0.26	-0.27 °C; -0.08	-1.55 °C; -0.37
	591 m; σ= 0.07	1020 m; σ= 0.04	999 m; σ= -0.01	979 m; σ= -0.02	27 m; σ= -0.03	46 m; σ= -0.11
EC-Earth3	-1.13 °C; -0.12	-0.65 °C; -0.14	-0.06 °C; -0.12	0.24 °C; -0.09	0.05 °C; -0.02	-0.82 °C; -0.09
	390 m; σ= 0.05	178 m; σ= -0.03	349 m; σ= -0.09	322 m; σ= -0.10	14 m; σ= -0.02	53 m; σ= 0.03
GFDL-CM4	-0.29 °C; 0.04	0.03 °C; 0.04	0.31 °C; 0.04	0.35 °C; 0.05	0.01 °C; -0.01	-0.09 °C; -0.10
	370 m; σ= 0.07	371 m; σ= 0.03	388 m; σ= 0.00	502 m; σ= 0.00	4 m; σ= -0.01	25 m; σ= -0.07
GFDL-ESM4	-0.59 °C; 0.12	-0.59 °C; 0.10	-0.43 °C; 0.12	-0.40 °C; 0.10	0.09 °C; 0.03	0.17 °C; -0.01
	256 m; σ= 0.17	337 m; σ= 0.16	655 m; σ= 0.15	408 m; σ= 0.12	9 m; σ= 0.01	47 m; σ= -0.03
GISS-E2-1-H	-1.50 °C; -0.56	-1.06 °C; -0.56	-0.82 °C; -0.65	-0.74 °C; -0.72	-0.20 °C; -0.19	-1.12 °C; -0.48
	402 m; σ= -0.26	417 m; σ= -0.32	280 m; σ= -0.42	64 m; σ= -0.48	19 m; σ= -0.12	68 m; σ= -0.25
IPSL-CM6A-LR	-0.80 °C; -0.05	-0.56 °C; -0.07	-0.26 °C; -0.08	-0.22 °C; -0.09	0.31 °C; -0.01	-0.75 °C; -0.08
	477 m; σ= 0.06	467 m; σ= 0.01	681 m; σ= -0.03	574 m; σ= -0.04	26 m; σ= -0.05	69 m; σ= 0.03
MIROC6	0.05 °C; 0.00	0.09 °C; -0.02	0.27 °C; -0.03	0.25 °C; -0.02	0.02 °C; -0.04	0.92 °C; -0.07
	338 m; σ= -0.01	390 m; σ= -0.03	473 m; σ= -0.05	517 m; σ= -0.04	20 m; σ= -0.03	126 m; σ= -0.19
MPI-ESM1-2-HR	-0.11 °C; -0.07	-0.32 °C; -0.11	-0.18 °C; -0.13	-0.08 °C; -0.09	0.07 °C; -0.07	-0.28 °C; -0.21
	214 m; σ= -0.04	271 m; σ= -0.05	448 m; σ= -0.08	507 m; σ= -0.06	18 m; σ= -0.06	34 m; σ= -0.13
MRI-ESM2-0	0.13 °C; 0.06	0.51 °C; 0.06	0.86 °C; 0.06	0.98 °C; 0.07	0.24 °C; 0.00	0.52 °C; -0.01
	756 m; σ= 0.03	891 m; σ= -0.01	1029 m; σ= -0.06	868 m; σ= -0.07	47 m; σ= -0.03	191 m; σ= -0.08
NorESM2-LM	-1.78 °C; 0.18	-1.46 °C; 0.18	-1.06 °C; 0.19	-0.93 °C; 0.21	-0.12 °C; 0.12	-0.59 °C; 0.07
	77 m; σ= 0.36	116 m; σ= 0.31	123 m; σ= 0.28	3 m; σ= 0.27	9 m; σ= 0.11	3 m; σ= 0.13
UKESM1-0-LL	-1.93 °C; -0.04	-1.78 °C; -0.05	-1.43 °C; -0.06	-1.28 °C; -0.05	-0.15 °C; 0.02	-0.94 °C; -0.04
	589 m; σ= 0.20	702 m; σ= 0.17	645 m; σ= 0.11	454 m; σ= 0.11	20 m; σ= 0.03	42 m; σ= 0.08
MMM	-0.71 °C; -0.03	-0.46 °C; -0.03	-0.14 °C; -0.03	-0.04 °C; -0.03	-0.02 °C; -0.06	-0.27 °C; -0.16
	476 m; σ= 0.06	545 m; σ= 0.03	611 m; σ= -0.01	516 m; σ= -0.02	23 m; σ= -0.05	62 m; σ= -0.10

TABLE A2. Area-weighted mean bias model minus WOA18 climatology in potential temperature (first line, left), salinity (first line, right; unit: psu) and density σ_2 (second line) of the Arctic deep water, defined here as properties at 2000 m depth, for each model and the multi-model mean "MMM" in the four deep basins.

Model	Nansen	Amundsen	Makarov	Canada
BCC-CSM2-MR	2.50 °C; 0.19 -0.15 kg m^{-3}	2.75 °C; 0.21 -0.17 kg m^{-3}	2.17 °C; 0.18 -0.12 kg m^{-3}	2.31 °C; 0.22 -0.10 kg m^{-3}
CAMS-CSM1-0	1.57 °C; -0.02 -0.19 kg m^{-3}	1.72 °C; -0.03 -0.22 kg m^{-3}	1.28 °C; -0.04 -0.18 kg m^{-3}	1.35 °C; -0.03 -0.18 kg m^{-3}
CESM2	2.20 °C; 0.07 -0.20 kg m^{-3}	2.27 °C; 0.06 -0.22 kg m^{-3}	1.83 °C; 0.04 -0.19 kg m^{-3}	1.83 °C; 0.05 -0.18 kg m^{-3}
CanESM5	-0.04 °C; -0.28 -0.22 kg m^{-3}	-0.12 °C; -0.30 -0.23 kg m^{-3}	-0.38 °C; -0.31 -0.20 kg m^{-3}	-0.51 °C; -0.35 -0.22 kg m^{-3}
EC-Earth3	1.16 °C; -0.07 -0.18 kg m^{-3}	1.14 °C; -0.09 -0.20 kg m^{-3}	0.86 °C; -0.09 -0.17 kg m^{-3}	0.88 °C; -0.09 -0.17 kg m^{-3}
GFDL-CM4	0.86 °C; 0.00 -0.10 kg m^{-3}	0.82 °C; -0.02 -0.10 kg m^{-3}	0.90 °C; -0.04 -0.13 kg m^{-3}	0.92 °C; -0.04 -0.13 kg m^{-3}
GFDL-ESM4	1.13 °C; 0.13 -0.02 kg m^{-3}	1.13 °C; 0.12 -0.03 kg m^{-3}	0.75 °C; 0.06 -0.04 kg m^{-3}	0.50 °C; 0.03 -0.03 kg m^{-3}
GISS-E2-1-H	0.28 °C; -0.29 -0.26 kg m^{-3}	0.29 °C; -0.42 -0.37 kg m^{-3}	-0.45 °C; -0.41 -0.28 kg m^{-3}	-0.72 °C; -0.47 -0.30 kg m^{-3}
IPSL-CM6A-LR	1.23 °C; -0.09 -0.21 kg m^{-3}	1.21 °C; -0.11 -0.22 kg m^{-3}	0.88 °C; -0.13 -0.20 kg m^{-3}	0.87 °C; -0.13 -0.20 kg m^{-3}
MIROC6	1.32 °C; -0.08 -0.21 kg m^{-3}	1.30 °C; -0.09 -0.22 kg m^{-3}	1.08 °C; -0.11 -0.21 kg m^{-3}	1.11 °C; -0.09 -0.20 kg m^{-3}
MPI-ESM1-2-HR	1.09 °C; -0.13 -0.22 kg m^{-3}	0.99 °C; -0.16 -0.24 kg m^{-3}	0.74 °C; -0.15 -0.20 kg m^{-3}	0.89 °C; -0.15 -0.22 kg m^{-3}
MRI-ESM2-0	2.45 °C; 0.01 -0.28 kg m^{-3}	2.45 °C; -0.01 -0.29 kg m^{-3}	2.13 °C; -0.03 -0.28 kg m^{-3}	2.13 °C; -0.04 -0.29 kg m^{-3}
NorESM2-LM	0.39 °C; 0.20 0.12 kg m^{-3}	0.33 °C; 0.19 0.12 kg m^{-3}	0.07 °C; 0.16 0.12 kg m^{-3}	0.00 °C; 0.17 0.14 kg m^{-3}
UKESM1-0-LL	0.22 °C; -0.09 -0.10 kg m^{-3}	0.15 °C; -0.11 -0.10 kg m^{-3}	-0.10 °C; -0.14 -0.10 kg m^{-3}	-0.14 °C; -0.15 -0.10 kg m^{-3}
MMM	1.14 °C; -0.04 -0.20 kg m^{-3}	1.14 °C; -0.06 -0.22 kg m^{-3}	0.87 °C; -0.07 -0.18 kg m^{-3}	0.89 °C; -0.07 -0.18 kg m^{-3}

TABLE A3. Area-weighted mean bias model minus WOA18 climatology in potential temperature (first line, left), salinity (first line, right; unit: psu), and density σ_2 (second line) of the bottom water, defined as the deepest grid cell with values, for each model and the multi-model mean "MMM" in the four deep basins and on the two shelf regions of interest.

Model	Nansen	Amundsen	Makarov	Canada	Sib. Shelf	Gre. Shelf
BCC-CSM2-MR	2.88 °C; 0.18 -0.20 kg m^{-3}	2.91 °C; 0.21 -0.18 kg m^{-3}	2.55 °C; 0.21 -0.14 kg m^{-3}	2.46 °C; 0.23 -0.12 kg m^{-3}	-0.47 °C; -1.79 -1.37 kg m^{-3}	-0.62 °C; -0.70 -0.49 kg m^{-3}
CAMS-CSM1-0	1.63 °C; -0.05 -0.22 kg m^{-3}	1.52 °C; -0.03 -0.19 kg m^{-3}	1.39 °C; -0.05 -0.19 kg m^{-3}	1.26 °C; -0.03 -0.17 kg m^{-3}	-0.06 °C; -3.07 -2.42 kg m^{-3}	0.53 °C; -0.89 -0.79 kg m^{-3}
CESM2	2.24 °C; 0.05 -0.22 kg m^{-3}	2.14 °C; 0.05 -0.21 kg m^{-3}	2.00 °C; 0.04 -0.21 kg m^{-3}	1.62 °C; 0.04 -0.16 kg m^{-3}	0.39 °C; 0.02 -0.06 kg m^{-3}	1.34 °C; 0.16 -0.05 kg m^{-3}
CanESM5	-0.19 °C; -0.25 -0.18 kg m^{-3}	-0.25 °C; -0.24 -0.17 kg m^{-3}	-0.42 °C; -0.34 -0.22 kg m^{-3}	-0.66 °C; -0.26 -0.14 kg m^{-3}	-0.31 °C; -0.93 -0.73 kg m^{-3}	-1.52 °C; -0.51 -0.24 kg m^{-3}
EC-Earth3	1.30 °C; -0.04 -0.17 kg m^{-3}	1.31 °C; -0.04 -0.17 kg m^{-3}	1.04 °C; -0.07 -0.17 kg m^{-3}	0.86 °C; -0.02 -0.11 kg m^{-3}	0.30 °C; 0.51 0.36 kg m^{-3}	-0.72 °C; -0.05 0.04 kg m^{-3}
GFDL-CM4	0.59 °C; -0.02 -0.08 kg m^{-3}	0.50 °C; -0.02 -0.07 kg m^{-3}	0.74 °C; -0.04 -0.11 kg m^{-3}	0.49 °C; -0.02 -0.07 kg m^{-3}	0.04 °C; -0.83 -0.68 kg m^{-3}	0.13 °C; -0.11 -0.11 kg m^{-3}
GFDL-ESM4	1.27 °C; 0.11 -0.05 kg m^{-3}	1.24 °C; 0.11 -0.05 kg m^{-3}	0.87 °C; 0.07 -0.04 kg m^{-3}	0.57 °C; 0.03 -0.04 kg m^{-3}	0.18 °C; -1.24 -1.01 kg m^{-3}	0.35 °C; -0.02 -0.07 kg m^{-3}
GISS-E2-1-H	0.08 °C; -0.20 -0.16 kg m^{-3}	0.07 °C; -0.37 -0.30 kg m^{-3}	-0.52 °C; -0.40 -0.26 kg m^{-3}	-0.83 °C; -0.43 -0.26 kg m^{-3}	-0.17 °C; -0.24 -0.17 kg m^{-3}	-1.01 °C; -0.39 -0.19 kg m^{-3}
IPSL-CM6A-LR	1.29 °C; -0.02 -0.16 kg m^{-3}	1.28 °C; -0.03 -0.16 kg m^{-3}	1.03 °C; -0.07 -0.17 kg m^{-3}	0.89 °C; -0.03 -0.13 kg m^{-3}	0.75 °C; 0.36 0.18 kg m^{-3}	-0.52 °C; -0.05 0.03 kg m^{-3}
MIROC6	1.22 °C; -0.11 -0.22 kg m^{-3}	1.18 °C; -0.11 -0.22 kg m^{-3}	1.04 °C; -0.12 -0.21 kg m^{-3}	1.14 °C; -0.10 -0.21 kg m^{-3}	0.08 °C; 0.00 -0.01 kg m^{-3}	1.22 °C; 0.10 -0.10 kg m^{-3}
MPI-ESM1-2-HR	1.18 °C; -0.17 -0.26 kg m^{-3}	1.01 °C; -0.20 -0.26 kg m^{-3}	0.92 °C; -0.19 -0.25 kg m^{-3}	0.96 °C; -0.17 -0.24 kg m^{-3}	0.09 °C; -1.34 -1.09 kg m^{-3}	-0.14 °C; -0.37 -0.28 kg m^{-3}
MRI-ESM2-0	2.39 °C; -0.05 -0.31 kg m^{-3}	2.33 °C; -0.05 -0.31 kg m^{-3}	2.20 °C; -0.04 -0.30 kg m^{-3}	2.10 °C; -0.05 -0.29 kg m^{-3}	0.45 °C; 0.31 0.18 kg m^{-3}	0.53 °C; -0.06 -0.11 kg m^{-3}
NorESM2-LM	0.66 °C; 0.41 0.25 kg m^{-3}	0.60 °C; 0.42 0.27 kg m^{-3}	0.12 °C; 0.17 0.12 kg m^{-3}	0.02 °C; 0.17 0.13 kg m^{-3}	-0.03 °C; -0.82 -0.66 kg m^{-3}	-0.35 °C; 0.16 0.18 kg m^{-3}
UKESM1-0-LL	0.26 °C; -0.11 -0.12 kg m^{-3}	0.22 °C; -0.12 -0.12 kg m^{-3}	-0.08 °C; -0.15 -0.11 kg m^{-3}	-0.15 °C; -0.16 -0.11 kg m^{-3}	-0.16 °C; -0.31 -0.25 kg m^{-3}	-0.87 °C; -0.06 0.05 kg m^{-3}
MMM	1.25 °C; -0.04 -0.18 kg m^{-3}	1.21 °C; -0.03 -0.18 kg m^{-3}	0.98 °C; -0.06 -0.18 kg m^{-3}	0.88 °C; -0.03 -0.13 kg m^{-3}	0.06 °C; -0.57 -0.45 kg m^{-3}	-0.24 °C; -0.06 -0.10 kg m^{-3}

References

Aagaard, K., 1981: On the deep circulation in the Arctic Ocean. *Deep Sea Research Part A. Oceanographic Research Papers*, **28**, 251–268, https://doi.org/10.1016/0198-0149(81)90066-2.

Aagaard, K., J. Swift, and E. Carmack, 1985: Thermohaline circulation in the Arctic Mediterranean sea. *Journal of Geophysical Research: Oceans*, **90**, 4833–4846, https://doi.org/10.1029/JC090iC03p04833.

Adcroft, A., and Coauthors, 2019: The GFDL global ocean and sea ice model OM4. 0: Model description and simulation features. *Journal of Advances in Modeling Earth Systems*, **11**, 3167–3211, https://doi.org/10.1029/2019MS001726.

Aksenov, Y., V. Ivanov, A. Nurser, S. Bacon, I. Polyakov, A. Coward, A. Naveira-Garabato, and A. Beszczynska-Moeller, 2011: The Arctic circumpolar boundary current. *Journal of Geophysical Research: Oceans*, **116**, https://doi.org/10.1029/2010JC006637.

Årthun, M., and T. Eldevik, 2016: On anomalous ocean heat transport toward the Arctic and associated climate predictability. *Journal of Climate*, **29**, 689–704, https://doi.org/10.1175/JCLI-D-15-0448.1.

Behrendt, A., H. H. Sumata, B. Rabe, and U. Schauer, 2018: UDASH–unified database for Arctic and Subarctic hydrography. *Earth System Science Data*, **10**, 1119–1138, https://doi.org/10.5194/essd-10-1119-2018.

Beszczynska-Möller, A., E. Fahrbach, U. Schauer, and E. Hansen, 2012: Variability in Atlantic water temperature and transport at the entrance to the Arctic Ocean, 1997–2010. *ICES Journal of Marine Science*, **69**, 852–863, https://doi.org/10.1093/icesjms/fss056.

Björk, G., M. Jakobsson, K. Assmann, L. Andersson, J. Nilsson, C. Stranne, and L. Mayer, 2018: Bathymetry and oceanic flow structure at two deep passages crossing the Lomonosov Ridge. *Ocean Science*, **14**, 1–13, https://doi.org/10.5194/os-14-1-2018.

Boucher, O., and Coauthors, 2020: Presentation and evaluation of the IPSL-CM6A-LR climate model. *Journal of Advances in Modeling Earth Systems*, **12**, e2019MS002 010, https://doi.org/10.1029/2019MS002010.

Chatterjee, S., R. Raj, L. Bertino, Ø. Skagseth, M. Ravichandran, and O. Johannessen, 2018: Role of Greenland Sea gyre circulation on Atlantic water temperature variability in the Fram Strait. *Geophysical Research Letters*, **45**, 8399–8406, https://doi.org/10.1029/2018GL079174.

Danabasoglu, G., J. Lamarque, J. Bacmeister, D. A. Bailey, A. K. DuVivier, J. Edwards, and L. K. Emmons et al., 2020: The community earth system model version 2 (CESM2). *Journal of Advances in Modeling Earth Systems*, **12**, https://doi.org/10.1029/2019MS001916.

Danabasoglu, G., W. Large, and B. Briegleb, 2010: Climate impacts of parameterized Nordic Sea overflows. *Journal of Geophysical Research: Oceans*, **115**, https://doi.org/10.1029/2010JC006243.

Davy, R., and S. Outten, 2020: The Arctic surface climate in CMIP6: status and developments since CMIP5. *Journal of Climate*, **33**, 8047–8068, https://doi.org/10.1175/JCLI-D-19-0990.1.

De Steur, L., E. Hansen, C. Mauritzen, A. Beszczynska-Möller, and E. Fahrbach, 2014: Impact of recirculation on the East Greenland Current in Fram Strait: Results from moored current meter measurements between 1997 and 2009. *Deep Sea Research Part I: Oceanographic Research Papers*, **92**, 26–40, https://doi.org/10.1016/j.dsr.2014.05.018.

Decloedt, T., and D. Luther, 2010: On a simple empirical parameterization of topography-catalyzed diapycnal mixing in the abyssal ocean. *Journal of physical oceanography*, **40**, 487–508, https://doi.org/10.1175/2009JPO4275.1.

Docquier, D., R. Fuentes-Franco, T. Koenigk, and T. Fichefet, 2020: Sea ice—ocean interactions in the barents sea modeled at different resolutions. *Frontiers in Earth Science*, **8**, 172, https://doi.org/10.3389/feart.2020.00172.

Docquier, D., and T. Koenigk, 2021: A review of interactions between ocean heat transport and arctic sea ice. *Environmental Research Letters*, **16**, 123 002, https://doi.org/10.1088/1748-9326/ac30be.

Docquier, D., and Coauthors, 2019: Impact of model resolution on arctic sea ice and north atlantic ocean heat transport. *Climate Dynamics*, **53 (7)**, 4989–5017, https://doi.org/10.1007/s00382-019-04840-y.

Döscher, R., M. Acosta, A. Alessandri, P. Anthoni, A. Arneth, T. Arsouze, T. Bergmann, and R. Bernadello et al., 2021: The EC-Earth3 Earth System Model for the Climate Model Intercomparison Project 6. *Geosci. Model Dev. Discuss.*, https://doi.org/10.5194/gmd-2020-446.

Dufour, C., A. Morrison, S. Griffies, I. Frenger, H. Zanowski, and M. Winton, 2017: Preconditioning of the Weddell Sea polynya by the ocean mesoscale and dense water overflows. *Journal of Climate*, **30**, 7719–7737, https://doi.org/10.1175/JCLI-D-16-0586.1.

Dunne, J., and Coauthors, 2020: The GFDL Earth System Model version 4.1 (GFDL-ESM 4.1): Overall coupled model description and simulation characteristics. *Journal of Advances in Modeling Earth Systems*, https://doi.org/10.1029/2019MS002015.

Environmental Working Group, 1997: Joint US-Russian atlas of the Arctic Ocean for the winter period. National Snow and Ice Data Center.

Environmental Working Group, 1998: Joint US-Russian atlas of the Arctic Ocean for the summer period. National Snow and Ice Data Center.

Eyring, V., S. Bony, G. Meehl, C. Senior, B. Stevens, R. Stouffer, and K. Taylor, 2016: Overview of the Coupled Model Intercomparison Project Phase 6 (CMIP6) experimental design and organization. *Geoscientific Model Development*, **9**, 1937–1958, https://doi.org/10.5194/gmd-9-1937-2016.

Fer, I., Z. Koenig, I. Kozlov, M. Ostrowski, T. Rippeth, L. Padman, A. Bosse, and E. Kolås, 2020: Tidally forced lee waves drive turbulent mixing along the Arctic Ocean margins. *Geophysical Research Letters*, **47**, e2020GL088 083, https://doi.org/10.1029/2020GL088083.

Fox-Kemper, B., and Coauthors, 2019: Challenges and prospects in ocean circulation models. *Frontiers in Marine Science*, **6**, 65, https://doi.org/10.3389/fmars.2019.00065.

Frank, M., W. Smethie Jr, and R. Bayer, 1998: Investigation of subsurface water flow along the continental margin of the Eurasian Basin using the transient tracers tritium, 3He, and CFCs. *Journal of Geophysical Research: Oceans*, **103**, 30 773–30 792, https://doi.org/10.1029/1998JC900003.

GEBCO Compilation Group, 2021: GEBCO 2021 Grid. doi:10.5285/c6612cbe-50b3-0cff-e053-6c86abc09f8f.

Good, S. A., M. J. Martin, and N. A. Rayner, 2013: EN4: quality controlled ocean temperature and salinity profiles and monthly objective analyses with uncertainty estimates. *Journal of Geophysical Research: Oceans*, **118**, 6704–6716, https://doi.org/10.1002/2013JC009067.

Griffies, S., and Coauthors, 2016: OMIP contribution to CMIP6: Experimental and diagnostic protocol for the physical component of the Ocean Model Intercomparison Project. *Geoscientific Model Development*, **9**, 3231–3296, https://doi.org/10.5194/gmd-9-3231-2016.

Heuzé, C., 2017: North Atlantic deep water formation and AMOC in CMIP5 models. *Ocean Science*, **13**, 609–622, https://doi.org/10.5194/os-13-609-2017.

Heuzé, C., 2021: Antarctic Bottom Water and North Atlantic Deep Water in CMIP6 models. *Ocean Science*, https://doi.org/10.5194/os-17-59-2021.

Hinrichs, C., Q. Wang, N. Koldunov, L. Mu, T. Semmler, D. Sidorenko, and T. Jung, 2021: Atmospheric wind biases: A challenge for simulating the arctic ocean in coupled models? *Journal of Geophysical Research: Oceans*, **126 (10)**, e2021JC017 565, https://doi.org/10.1029/2021JC017565.

Huang, C., F. Qiao, and D. Dai, 2014: Evaluating CMIP5 simulations of mixed layer depth during summer. *Journal of Geophysical Research: Oceans*, **119**, 2568–258, https://doi.org/10.1002/2013JC009535.

Ilıcak, M., and Coauthors, 2016: An assessment of the Arctic Ocean in a suite of interannual CORE-II simulations. Part III: Hydrography and fluxes. *Ocean Modelling*, **100**, 141–161, https://doi.org/10.1016/j.ocemod.2016.02.004.

IPCC, 2019: *IPCC Special Report on the Ocean and Cryosphere in a Changing Climate*. Cambridge University Press.

IPCC, 2021: *Climate Change 2021: The Physical Science Basis. Contribution of Working Group I to the Sixth Assessment Report of the Intergovernmental Panel on Climate Change*. Cambridge University Press.

Ivanov, V., G. Shapiro, J. Huthnance, D. Aleynik, and P. Golovin, 2004: Cascades of dense water around the world ocean. *Progress in oceanography*, **60**, 47–98, https://doi.org/10.1016/j.pocean.2003.12.002.

Karcher, M., F. Kauker, R. Gerdes, E. Hunke, and J. Zhang, 2007: On the dynamics of atlantic water circulation in the arctic ocean. *Journal of Geophysical Research: Oceans*, **112 (C4)**, https://doi.org/10.1029/2006JC003630.

Kelley, M., and Coauthors, 2020: GISS-E2. 1: Configurations and climatology. *Journal of Advances in Modeling Earth Systems*, https://doi.org/10.1029/2019MS002025.

Khosravi, N., Q. Wang, N. Koldunov, C. Hinrichs, T. Semmler, S. Danilov, and T. Jung, 2022: The Arctic Ocean in CMIP6 models: Biases and projected changes in temperature and salinity. *Earth's Future*, e2021EF002282, https://doi.org/10.1029/2021EF002282.

Korhonen, M., B. Rudels, M. Marnela, A. Wisotzki, and J. Zhao, 2013: Time and space variability of freshwater content, heat content and seasonal ice melt in the Arctic Ocean from 1991 to 2011. *Ocean Science*, **9**, 1015–1055, https://doi.org/10.5194/os-9-1015-2013.

Kraus, E., 1990: Diapycnal mixing. *Climate-Ocean Interaction*, 269–293, https://doi.org/10.1007/978-94-009-2093-4_14.

Kwok, R., 2018: Arctic sea ice thickness, volume, and multiyear ice coverage: losses and coupled variability (1958–2018). *Environmental Research Letters*, **13**, 105 005, https://doi.org/10.1088/1748-9326/aae3ec.

Langehaug, H., and E. Falck, 2012: Changes in the properties and distribution of the intermediate and deep waters in the Fram Strait. *Progress in Oceanography*, **96**, 57–76, https://doi.org/10.1016/j.pocean.2011.10.002.

Large, W., J. McWilliams, and S. Doney, 1994: Oceanic vertical mixing: A review and a model with a non local boundary layer parameterization. *Reviews of geophysics*, **32**, 363–403, https://doi.org/10.1029/94RG01872.

Lavoie, J., B. Tremblay, and E. Rosenblum, 2022: Pacific Waters Pathways and Vertical Mixing in the CESM1-LE: Implication for Mixed Layer Depth Evolution and Sea Ice Mass Balance in the Canada Basin. *Journal of Geophysical Research: Oceans*, **127**, e2021JC017 729, https://doi.org/10.1029/2021JC017729.

Lique, C., and M. Thomas, 2018: Latitudinal shift of the Atlantic Meridional Overturning Circulation source regions under a warming climate. *Nature Climate Change*, **8**, 1013–1020, https://doi.org/10.1038/s41558-018-0316-5.

Locarnini, R., and Coauthors, 2018: *World Ocean Atlas 2018, Volume 1: Temperature*. A. Mishonov Technical Ed.; NOAA Atlas NESDIS 81.

Luneva, M., V. Ivanov, F. Tuzov, Y. Aksenov, J. Harle, S. Kelly, and J. Holt, 2020: Hotspots of dense water cascading in the Arctic Ocean: Implications for the Pacific water pathways. *Journal of Geophysical Research: Oceans*, **125**, e2020JC016 044, https://doi.org/10.1029/2020JC016044.

Madec, G., 2008: NEMO Ocean Engine. Note du Pôle de Modélisation, vol. 27. Tech. rep., Inst. Pierre-Simon Laplace, Paris.

Manucharyan, G., and M. Spall, 2016: Wind driven freshwater build-up and release in the Beaufort Gyre constrained by mesoscale eddies. *Geophysical Research Letters*, **43**, 273–282, https://doi.org/10.1002/2015GL065957.

Marnela, M., B. Rudels, I. Goszczko, A. Beszczynska-Möller, and U. Schauer, 2016: Fram Strait and Greenland Sea transports, water masses, and water mass transformations 1999–2010 (and beyond). *Journal of Geophysical Research: Oceans*, **121**, 2314–2346, https://doi.org/10.1002/2015JC011312.

McDougall, T., and P. Barker, 2011: Getting started with TEOS-10 and the Gibbs Seawater (GSW) Oceanographic Toolbox. Tech. rep., OR/IAPSO WG127.

Mohrmann, M., C. Heuzé, and S. Swart, 2021: Southern Ocean polynyas in CMIP6 models. *The Cryosphere*, **15**, 4281–4313, https://doi.org/10.5194/tc-15-4281-2021.

Morison, J., C. Long, and M. Levine, 1985: Internal wave dissipation under sea ice. *Journal of Geophysical Research*, **90**, 959–966, https://doi.org/10.1029/JC090iC06p11959.

Muilwijk, M., L. Smedsrud, M. Ilıcak, and H. Drange, 2018: Atlantic Water heat transport variability in the 20th century Arctic Ocean from a global ocean model and observations. *Journal of Geophysical Research: Oceans*, **123**, 8159–8179, https://doi.org/10.1029/2018JC014327.

Muilwijk, M., L. Smedsrud, I. Polyakov, A. Nummelin, C. Heuzé, and H. Zanowski, subm.: Divergence in climate model projections of future Arctic Ocean stratification. *Journal of Climate*.

Muilwijk, M., and Coauthors, 2019: Arctic Ocean response to Greenland Sea wind anomalies in a suite of model simulations. *Journal of Geophysical Research: Oceans*, **124**, 6286–6322, https://doi.org/10.1029/2019JC015101.

Müller, W., and Coauthors, 2018: A Higher-resolution Version of the Max Planck Institute Earth System Model (MPI-ESM1. 2-HR). *Journal of Advances in Modeling Earth Systems*, **10**, https://doi.org/10.1029/2017MS001217.

Nansen, F., 1906: Northern waters: Captain Roald Amundsen's oceanographic observations in the Arctic Seas in 1901. With a discussion of the origin of the Bottom-Waters of the Northern Seas (No. 3). In commission by Jacob Dybwad.

Noh, Y., and H. Jin Kim, 1999: Simulations of temperature and turbulence structure of the oceanic boundary layer with the improved near-surface process. *Journal of Geophysical Research: Oceans*, **104**, 15 621–15 634, https://doi.org/10.1029/1999JC900068.

Notz, D., A. Jahn, M. Holland, E. Hunke, F. Massonnet, J. Stroeve, B. Tremblay, and M. Vancoppenolle, 2016: The CMIP6 Sea-Ice Model Intercomparison Project (SIMIP): understanding sea ice through climate-model simulations. *Geoscientific Model Development*, **9**, 3427–3446, https://doi.org/10.5194/gmd-9-3427-2016.

Notz, D., and SIMIP Community, 2020: Arctic sea ice in CMIP6. *Geophysical Research Letters*, **47**, e2019GL086 749, https://doi.org/10.1029/2019GL086749.

Onarheim, I., T. Eldevik, L. Smedsrud, and J. Stroeve, 2018: Seasonal and regional manifestation of Arctic sea ice loss. *Journal of Climate*, **31**, 4917–4932, https://doi.org/10.1175/JCLI-D-17-0427.1.

Pacanowski, R., and S. Philander, 1981: Parameterization of vertical mixing in numerical models of tropical oceans. *Journal of Physical Oceanography*, **11**, 1443–1451, https://doi.org/10.1175/1520-0485(1981)011<1443:POVMIN>2.0.CO;2.

Peralta-Ferriz, C., and R. Woodgate, 2015: Seasonal and interannual variability of pan-Arctic surface mixed layer properties from 1979 to 2012 from hydrographic data, and the dominance of stratification for multiyear mixed layer depth shoaling. *Progress in Oceanography*, **134**, 19–53, https://doi.org/10.1016/j.pocean.2014.12.005.

Pinkel, R., 2005: Near-inertial wave propagation in the western Arctic. *Journal of Physical Oceanography*, **35**, 645–665, https://doi.org/10.1175/JPO2715.1.

Pnyushkov, A., I. Polyakov, V. Ivanov, Y. Aksenov, A. Coward, M. Janout, and B. Rabe, 2015: Structure and variability of the boundary current in the eurasian basin of the arctic ocean. *Deep Sea Research Part I: Oceanographic Research Papers*, **101**, 80–97, https://doi.org/10.1016/j.dsr.2015.03.001.

Polyakov, I., and Coauthors, 2017: Greater role for Atlantic inflows on sea-ice loss in the Eurasian Basin of the Arctic Ocean. *Science*, **356**, 285–291, https://doi.org/10.1126/science.aai8204.

Polyakov, I., and Coauthors, 2020: Weakening of cold halocline layer exposes sea ice to oceanic heat in the eastern Arctic Ocean. *Journal of Climate*, **33**, 107–123, https://doi.org/0.1175/JCLI-D-19-0976.1.

Rabe, B., and Coauthors, 2022: Overview of the MOSAiC expedition: Physical oceanography. *Elementa: Science of the Anthropocene*, **10**, 00 062, https://doi.org/10.1525/elementa.2021.00062.

Rayner, N. A., D. E. Parker, E. B. Horton, C. K. Folland, L. V. Alexander, D. P. Rowell, E. C. Kent, and A. Kaplan, 2003: Global analyses of sea surface temperature, sea ice, and night marine air temperature since the late nineteenth century. *Journal of Geophysical Research*, **108**, 4407, https://doi.org/10.1029/2002JD002670.

Reichl, B., and R. Hallberg, 2018: A simplified energetics based planetary boundary layer (ePBL) approach for ocean climate simulations. *Ocean Modelling*, **132**, 112–129, https://doi.org/10.1016/j.ocemod.2018.10.004.

Rippeth, T., and E. Fine, 2022: Turbulent mixing in a changing Arctic Ocean. *Oceanography*, **35**, 11, https://doi.org/10.5670/oceanog.2022.103.

Rippeth, T., B. Lincoln, Y.-D. Lenn, J. Green, A. Sundfjord, and S. Bacon, 2015: Tide mediated warming of Arctic halocline by Atlantic heat fluxes over rough topography. *Nature Geoscience*, **8**, 191–194, https://doi.org/10.1038/ngeo2350.

Roberts, M. J., H. T. Hewitt, P. Hyder, D. Ferreira, S. A. Josey, M. Mizielinski, and A. Shelly, 2016: Impact of ocean resolution on coupled air-sea fluxes and large-scale climate. *Geophysical Research Letters*, **43 (19)**, 10–430, https://doi.org/10.1002/2016GL070559.

Rong, X. Y., J. Li, and H. M. Chen, 2019: Introduction of CAMS-CSM model and its participation in CMIP6. *Climate Change Res.*, **6**, https://doi.org/10.12006/j.issn.1673-1719.2019.186.

Rosenblum, E., R. Fajber, J. C. Stroeve, S. T. Gille, L. B. Tremblay, and E. C. Carmack, 2021: Surface salinity under transitioning ice cover in the Canada Basin: Climate model biases linked to vertical distribution of fresh water. *Geophysical Research Letters*, **48**, e2021GL094 739, https://doi.org/10.1029/2021GL094739.

Rudels, B., 1986: The θ-S relations in the northern seas: Implications for the deep circulation. *Polar Research*, **4**, 133–159, https://doi.org/0.3402/polar.v4i2.6928.

Rudels, B., 2009: *Encyclopedia of ocean sciences, 2nd ed.*, chap. Arctic Ocean circulation. Oxford, UK: Academic Pres.

Rudels, B., 2012: Arctic Ocean circulation and variability – advection and external forcing encounter constraints and local processes. *Ocean Science*, **8**, 261–286, https://doi.org/10.5194/os-8-261-2012.

Rudels, B., G. Björk, R. Muench, and U. Schauer, 1999: Double-diffusive layering in the Eurasian Basin of the Arctic Ocean. *Journal of Marine Systems*, **21**, 3–27, https://doi.org/10.1016/S0924-7963(99)00003-2.

Rudels, B., and D. Quadfasel, 1991: Convection and deep water formation in the Arctic Ocean-Greenland Sea system. *Journal of Marine Systems*, **2**, 435–450, https://doi.org/10.1016/0924-7963(91)90045-V.

Schauer, U., and A. Beszczynska-Möller, 2009: Problems with estimation and interpretation of oceanic heat transport – conceptual remarks for the case of Fram Strait in the Arctic Ocean. *Ocean Science*, **5**, 487–494, https://doi.org/10.5194/os-5-487-2009.

Schauer, U., E. Fahrbach, S. Osterhus, and G. Rohardt, 2004: Arctic warming through the Fram Strait: Oceanic heat transport from 3 years of measurements. *Journal of Geophysical Research: Oceans*, **109**, https://doi.org/10.1029/2003JC001823.

Schlosser, P., and Coauthors, 1997: The first trans-Arctic 14C section: comparison of the mean ages of the deep waters in the Eurasian and Canadian basins of the Arctic Ocean. *Nuclear Instruments and Methods in Physics Research Section B: Beam Interactions with Materials and Atoms*, **123**, 431–437, https://doi.org/10.1016/S0168-583X(96)00677-5.

Schmidtko, S., G. Johnson, and J. Lyman, 2013: MIMOC: A global monthly isopycnal upper-ocean climatology with mixed layers. *Journal of Geophysical Research: Oceans*, **118**, 1658–1672, https://doi.org/10.1002/jgrc.20122.

Seland, Ø., and Coauthors, 2020: Overview of the Norwegian Earth System Model (NorESM2) and key climate response of CMIP6 DECK, historical, and scenario simulations. *Geoscientific Model Development*, **13**, 6165–6200, https://doi.org/10.5194/gmd-13-6165-2020.

Sellar, A., and Coauthors, 2019: UKESM1: Description and evaluation of the UK Earth System Model. *Journal of Advances in Modeling Earth Systems*, **11**, 4513–4558, https://doi.org/10.1029/2019MS001739.

Shu, Q., Q. Wang, J. Su, X. Li, and F. Qiao, 2019: Assessment of the Atlantic water layer in the Arctic Ocean in CMIP5 climate models. *Climate Dynamics*, **53**, 5279–5291, https://doi.org/10.1007/s00382-019-04870-6.

Smedsrud, L., and Coauthors, 2022: Nordic Seas heat loss, Atlantic inflow, and Arctic sea ice cover over the last century. *Reviews of Geophysics*, **60**, e2020RG000 725, https://doi.org/10.1029/2020RG000725.

Smethie, W., D. Chipman, J. Swift, and K. Koltermann, 1988: Chlorofluoromethanes in the Arctic Mediterranean seas: Evidence for formation of bottom water in the Eurasian Basin and deep-water exchange through Fram Strait. *Deep Sea Research Part A Oceanographic Research Papers*, **35**, 347–369, https://doi.org/10.1016/0198-0149(88)90015-5.

Solomon, A., and Coauthors, 2021: Freshwater in the Arctic Ocean 2010–2019. *Ocean Science*, **17**, 1081–1102, https://doi.org/10.5194/os-17-1081-2021.

Spall, M., R. Pickart, P. Fratantoni, and A. Plueddemann, 2008: Western Arctic shelf break eddies: Formation and transport. *Journal of Physical Oceanography*, **38**, 644–668, https://doi.org/10.1175/2007JPO3829.1.

Steele, M., R. Morley, and W. Ermold, 2001: PHC: A global ocean hydrography with a high-quality Arctic Ocean. *Journal of Climate*, **14**, 2079–2087, https://doi.org/10.1175/1520-0442(2001)014<2079:PAGOHW>2.0.CO;2.

Swart, N., and Coauthors, 2019: The Canadian Earth System Model version 5 (CanESM5. 0.3). *Geoscientific Model Development*, **12**, https://doi.org/10.5194/gmd-2019-177.

Talandier, C., and Coauthors, 2014: Improvements of simulated Western North Atlantic current system and impacts on the AMOC. *Ocean Modelling*, **76**, 1–19, https://doi.org/10.1016/j.ocemod.2013.12.007.

Tamura, T., and K. Ohshima, 2011: Mapping of sea ice production in the Arctic coastal polynyas. *Journal of Geophysical Research: Oceans*, **116**, https://doi.org/10.1029/2010JC006586.

Tanhua, T., E. Jones, E. Jeansson, S. Jutterström, W. S. Jr, D. Wallace, and L. Anderson, 2009: Ventilation of the Arctic Ocean: Mean ages and inventories of anthropogenic CO2 and CFC-11. *Journal of Geophysical Research: Oceans*, **114**, https://doi.org/10.1029/2008JC004868.

Tatebe, H., and Coauthors, 2019: Description and basic evaluation of simulated mean state, internal variability, and climate sensitivity in MIROC6. *Geoscientific Model Development*, **12**, https://doi.org/10.5194/gmd-12-2727-2019.

Timmermans, M., and C. Garrett, 2006: Evolution of the deep water in the Canadian Basin in the Arctic Ocean. *Journal of physical oceanography*, **36**, 866–874, https://doi.org/10.1175/JPO2906.1.

Timmermans, M., P. Winsor, and J. Whitehead, 2005: Deep-water flow over the Lomonosov Ridge in the Arctic Ocean. *Journal of physical oceanography*, **35**, 1489–1493, https://doi.org/10.1175/JPO2765.1.

Valk, O., and Coauthors, 2020: Decrease in 230Th in the Amundsen Basin since 2007: far-field effect of increased scavenging on the shelf? *Ocean Science*, **16**, 221–234, https://doi.org/10.5194/os-16-221-2020.

von Appen, W., T. Baumann, M. Janout, N. Koldunov, Y. Lenn, R. Pickart, R. Scott, and Q. Wang, 2022: Eddies and the distribution of Eddy Kinetic Energy in the Arctic Ocean. *Oceanography*, **35**, https://doi.org/10.5670/oceanog.2022.122.

von Appen, W., U. Schauer, R. Somavilla, E. Bauerfeind, and A. Beszczynska-Möller, 2015: Exchange of warming deep waters across Fram Strait. *Deep Sea Research Part I: Oceanographic Research Papers*, **103**, 86–100, https://doi.org/10.1016/j.dsr.2015.06.003.

Wang, Q., C. Wekerle, S. Danilov, X. Wang, and T. Jung, 2018: A 4.5 km resolution Arctic Ocean simulation with the global multi-resolution model FESOM 1.4. *Geoscientific Model Development*, **11**, 1229–1255, https://doi.org/10.5194/gmd-11-1229-2018.

Wang, Q., and Coauthors, 2020: Intensification of the Atlantic Water supply to the Arctic Ocean through Fram Strait induced by Arctic sea ice decline. *Geophysical Research Letters*, **47**, e2019GL086 682, https://doi.org/10.1029/2019GL086682.

Woodgate, R., K. Aagaard, R. Muench, J. Gunn, G. Björk, B. Rudels, A. Roach, and U. Schauer, 2001: The Arctic Ocean boundary current along the Eurasian slope and the adjacent Lomonosov Ridge: Water mass properties, transports and transformations from moored instruments. *Deep Sea Research Part I: Oceanographic Research Papers*, **48**, 1757–1792, https://doi.org/10.1016/S0967-0637(00)00091-1.

Wu, T., and Coauthors, 2019: The Beijing Climate Center Climate System Model (BCC-CSM): the main progress from CMIP5 to CMIP6. *Geoscientific Model Development*, **12**, https://doi.org/10.5194/gmd-12-1573-2019.

Yukimoto, S., and Coauthors, 2019: The Meteorological Research Institute Earth System Model version 2.0, MRI-ESM2. 0: Description and basic evaluation of the physical component. *Journal of the Meteorological Society of Japan*, https://doi.org/10.2151/jmsj.2019-051.

Zanowski, H., A. Jahn, and M. Holland, 2021: Arctic Ocean Freshwater in CMIP6 Ensembles: Declining Sea Ice, Increasing Ocean Storage and Export. *Journal of Geophysical Research: Oceans*, **126**, e2020JC016 930, https://doi.org/10.1029/2020JC016930.

Zweng, M., and Coauthors, 2018: *World Ocean Atlas 2018, Volume 2: Salinity*. A. Mishonov Technical Ed.; NOAA Atlas NESDIS 82.